Studying Novel Material Properties Using Synchrotron-based Soft X-ray Spectroscopy

A Thesis Submitted to the

College of Graduate Studies and Research

in Partial Fulfillment of the Requirements

for the degree of Master of Science

in the Department of Physics and Engineering Physics

University of Saskatchewan

Saskatoon

By

Amy L. Pitman

Permission to Use

In presenting this thesis in partial fulfilment of the requirements for a Postgraduate degree from the University of Saskatchewan, I agree that the Libraries of this University may make it freely available for inspection. I further agree that permission for copying of this thesis in any manner, in whole or in part, for scholarly purposes may be granted by the professor or professors who supervised my thesis work or, in their absence, by the Head of the Department or the Dean of the College in which my thesis work was done. It is understood that any copying or publication or use of this thesis or parts thereof for financial gain shall not be allowed without my written permission. It is also understood that due recognition shall be given to me and to the University of Saskatchewan in any scholarly use which may be made of any material in my thesis.

Requests for permission to copy or to make other use of material in this thesis in whole or part should be addressed to:

Head of the Department of Physics and Engineering Physics

163 Physics Building

116 Science Place

University of Saskatchewan

Saskatoon, Saskatchewan

Canada

S7N 5E2

Abstract

This thesis is centred around the study materials with novel electronic properties, including transition metals interacting with semiconductors and unique molecular systems. The idea of advancing modern computing is the basis for motivating the work in that the projects all have potential to be used in novel applications that would impact the efficiency and/or execution of current technology. We have studied two variations of transition metals as they appear in materials and two molecular systems. As for the transition metals interacting with semiconductors, we first discuss transition metal atoms introduced as impurities to a semiconductor lattice, and second, we discuss transition metal oxides that are naturally semiconducting.

We have used a number of experimental and theoretical techniques to better understand these groups of materials. Materials prepared through high quality synthesis techniques were studied using x-ray spectroscopy made possible by synchrotron light sources. Computational software then allowed for the experiments to be interpreted by comparing them to the simulations.

In the study of transition metals as impurities, we chose the Co:MoS_2 system because MoS_2 has had promising results with other transition metal dopants. We examined the electronic structure for two purposes: (1) to determine the local bonding environment and locations of the cobalt atoms in order to better understand the behaviour of Co as an impurity; and (2) the overall band gap of the system so that we could evaluate the system's potential for use in applications. Experimental results combined with our theoretical simulations led us to conclude that the samples available were all metallic, and at low concentrations cobalt

atoms were able to substitute directly into the MoS_2 lattice.

An examination of copper (II) oxide allowed us to investigate the ability to tune the band gap of a known semiconductor through a synthesis process that applied axial pressure to the sample. For a collection of samples prepared at different pressures, x-ray spectroscopy methods showed an increasing band gap with increasing synthesis pressure, a result that is most encouraging for the field of band gap engineering.

Using soft x-ray spectroscopy to examine the conduction and valence bands of the two molecular systems, the potassium-doped hydrocarbons and Li_2RuO_3, was important for drawing conclusions about the materials' composition and behaviour. Results showed the introduction of new states at the lower edge of the conduction band of K:phenanthrene, a possible reason for its low-temperature superconductivity. Li_2RuO_3's electronic structure was examined and compared to calculations performed by collaborators.

Acknowledgements

The fields of condensed matter physics and synchrotron science often require incredible amounts of collaboration to achieve meaningful development. The work in this thesis is no different – it is a product of contributions to both experiments and morale that were crucial for the success of the projects within. Here I acknowledge those who gave their assistance to make these accomplishments a success.

First and foremost, I would like to thank my supervisor, Dr. Alex Moewes, for his guidance and support through my 4 years working as first an undergraduate summer student and then as a graduate student. His enthusiasm for synchrotron science and condensed matter physics is contagious and was an essential part of what led me to begin my work in this field. Most of all, I appreciate that he always found the right take on a project that allowed my interests to flow freely, making my work that much more enjoyable.

Both projects in this work required a great deal of reliance on collaborators to provide high quality samples and supplementary experimental data, as well as general insight and project motivation. Specifically, I would like to thank Dr. Ernst Kurmaev, Dr. Mikhail Uimin, Dr. Vitaly P. Pilyugin, Dr. Boris A. Gizhevskii, and those research assistants who had a hand in synthesis and experiments outside of my own synchrotron studies.

To name every member of Professor Moewes' research group, "The Beamteam", who guided me and answered my questions would take the majority of this page. As such, I simply wish to thank all past and present members of the Beamteam who were always ready and willing to help in any way possible.

The majority of my experimental work took place at the REIXS beamline at the Canadian

Light Source and at BL8 at the Advanced Light Source. I am incredibly grateful to the staff from both facilities who made the experiments possible, specifically, Dr. David Muir from the CLS and Dr. Wanli Yang from the ALS.

None of this work would have been undertaken without the generous financial support from a variety of sources, and I thank each for their contributions. These sources include the Natural Science and Engineering Research Council of Canada (NSERC), the Canada Research Chair program, and the University of Saskatchewan.

Finally, I wish to thank my family from the bottom of my heart. The constant support from my husband, Colin, and my parents has been crucial to my success, allowing me to feel confidence in my work and providing me with motivation when I needed it. Together, they have given me the belief that I can pursue and have success in any of my endeavours.

Dedicated to Colin, who supported and believed in me

through the entirety of my studies;

and to my parents, who taught me that I could do anything.

Contents

List of Tables

List of Figures

List of Abbreviations

ALS	Advanced Light Source
BL8	Beamline 8.0.1 (at ALS)
CB	Conduction Band
CBM	Conduction Band Minimum
CFM	Crystal Field Model
CLS	Canadian Light Source
CT	Charge Transfer
DFT	Density Functional Theory
DMS	Dilute Magnetic Semiconductor
DOS	Density Of States
EELS	Electron Energy Loss Spectroscopy
GGA	Generalized Gradient Approximation
HAP	High Axial Pressure
HOMO	Highest Occupied Molecular Orbital
HPT	High Pressure Torsion
LOF	List of Figures
LOT	List of Tables
LUMO	Lowest Unoccupied Molecular Orbital
MH	Mott Hubbard
MXCD	Magnetic X-ray Circular Dichroism
NEXAFS	Near Edge X-ray Absorption Fine Structure
NXES	Non-resonant X-ray Emission Spectroscopy
PFY	Partial Fluorescence Yield
REIXS	Resonant Elastic and Inelastic X-ray Scattering (beamline at CLS)
RIXS	Resonant Inelastic X-ray Scattering
SGM	Spherical Grating Monochromator
SIAM	Single Impurity Anderson Model
TEY	Total Electron Yield
TFY	Total Fluorescence Yield
UDD	Ultra-Dispersed Diamond
UMO	Unoccupied Molecular Orbital
VB	Valence Band
VBM	Valence Band Maximum
XAS	X-ray Absorption Spectroscopy
XES	X-ray Emission Spectroscopy
XRD	X-Ray Diffraction

Chapter 1

Introduction

I think science has enjoyed an extraordinary success because it has such a limited and narrow realm in which to focus its efforts. Namely, the physical universe.

– KEN JENKINS

Since the development of modern scientific and experimental techniques, the discovery and subsequent utilization of semiconductor materials has undoubtedly had the greatest impact on revolutionizing technology and our world. Once mankind developed an understanding of energy bands and band gaps in the 1920s and 1930s, utilization of semiconductor materials raced on at full speed. At Bell Labs in 1947, the first semiconductor application, the *transistor*, was developed. Subsequently, modern computing came into being, and we now find ourselves in a world surrounded by semiconductor technology [1]. Semiconductors can be found in computers, solar panels, cellular devices, even watches, and the capabilities of these devices are continually advancing. The spirit of furthering our understanding of semicon-

ductors and growing their applications motivates the theme of this thesis – to develop and improve materials for use in electronics.

Despite the success developers have had in the semiconductor industry, there is always a motivation to solve computational problems of greater difficulty. These might be theoretical calculations predicting the next fundamental particle like the Higgs Boson or mathematical modelling of the mutation of cancer cells. Regardless of why we needed faster computation, we have continued to make improvements to meet these goals, resulting in computer performance roughly doubling every two years. More commonly known as *Moore's Law*, this exponential trend follows a famous observation and subsequent prediction made by Gordon Moore [2] in 1965. He noticed that up to that point in time the number of components on an integrated circuit had doubled nearly every two years. Given that it had already kept up for more than a decade, he predicted that it would continue into the foreseeable future. Unbelievably, this trend has continued for more than forty years.

Achieving the Moore's Law trend in reality has generally been through a continual decrease in size of the constituent components so they can be placed at higher densities. Unfortunately, this may not last another decade because we are fast approaching the atomic limit. Simply put, we cannot make transistors smaller than a few dozen atoms because a small enough collection of atoms will no longer exhibit the bulk material properties required for operation. Clearly, a new approach is required if computing technology is needed to continually advance over the coming decades.

1.1 Transition Metals and Semiconductors

With our theme in mind, we focus on materials with novel properties due to the inclusion of transition metal elements. Specifically, we examine two ways in which transition metals appear in semiconductor applications: the addition of a transition metal as a dopant to a known semiconductor lattice; and transition metal oxides. Both cases can be examined using the same experimental techniques, evidence of further connection between the two projects.

Our examination involves x-ray absorption, resonant inelastic x-ray scattering, and x-ray emission measurements at several element-specific edges along with the use of multiplet calculations (see Section 3.6) to model the transition metal edge. Such modelling leads to a better understanding of the material and insight that wouldn't normally be found using only experimental data. Matching the model with the experiment further allows one to extract parameters such as the coordination of the dopant environment and the valency. Finally, the band gap, an important property in describing semiconductors, is determined from x-ray absorption and emission spectra and evaluated for changes related to the synthesis process.

1.1.1 Dilute Magnetic Semiconductors

Ideally, being able to detect and manipulate the spin of electrons would allow for technology to continue to advance at its current pace – at least for the near future – by utilizing the new states electron spin unlocks. Whether this will be a sustainable technology on its own or merely provide the time needed for further innovation is yet to be seen. Devices made specifically with detection and/or control of spin in mind have been coined spin electronics,

also referred to as *spintronics* [3, 4]. The most common spintronic devices are known as spin transistors and work similarly to regular transistors, except for the addition of another spin-controlled gate. With the additional gate, each bit would have four states made from combinations of high or low voltage and up or down spin.

Although the concept seems simple, finding materials that allow for control of electron spin while maintaining semiconducting properties has been a challenge for a number of years. The most recent success has been with the group of materials known as ferromagnetic semiconductors whose properties allow for easy incorporation into existing transistor technology while adding magnetic control of electron spin [5, 6]. However, these materials rarely have a Curie temperature at or above room temperature, severely limiting their spin control capabilities for consumer electronics operating at room temperature.

Finally, we turn to yet another class of materials – dilute magnetic semiconductors (DMSs). These fabricated materials begin with a known semiconductor and introduce transition metal atom impurities into the lattice. Some of the first studies used GaAs with Mn impurities [7], proving that certain semiconductors would willingly accept transition metals into their lattice. Since then, a number of combinations have been tried, including semiconducting oxides with transition metal doping [8]. A number of recent studies have shown manganese and cobalt in III-V and II-VI semiconductors to have great potential for being semiconducting room-temperature DMSs [3, 5, 6, 9–13]. Since the discovery of spintronics, MoS_2 has been one of the most used semiconductors used in the testing of DMSs. It has already shown the ability to be doped with Re [14], Ti [15], Cr [16], and Mn [17]. Ramasubramaniam *et. al.* performed in-depth examination of manganese doping in MoS_2, showing that very specific exchange interactions are key for magnetic ordering and that dopant con-

centrations between 10–15% lead to room-temperature ferromagnetism [18].

Despite the popularity of this stream of research, MoS_2 has yet to be tested with many possible transition metals, including cobalt. As such, we undertake the study of MoS_2 doped with cobalt as the primary system of interest for this work. It is important to note that when referring to doping in DMS materials, it is on a vastly different scale (several orders of magnitude larger) than doping in the semiconductor industry. Samples of varying cobalt doping have been prepared, ranging from the lower extreme of ≈10 wt% to the higher extreme of 25 wt%, as well as a sample variant that includes ultra-dispersed diamond (UDD), Co:UDD:MoS_2 in the ratio of 1:3:3.

Our study focuses on two particular investigations. The primary goal of this project is to determine the behaviour and location of the cobalt dopant atoms via the local bonding environment (see section 3.6 for further details). Secondly, we aim to investigate if the semiconducting properties are maintained after the inclusion of the transition metal and to analyse the relationship between semiconducting properties and dopant concentration. In achieving these goals, we gain further insight into the behaviour of transition metal atoms in host materials.

1.1.2 Transition Metal Oxides

Transition metal oxides inherently have a wide variety of surface structures allowing them to be used in a variety of novel applications. Both their catalytic and semiconducting properties are easily influenced by the presence of defects and exposure to electromagnetic radiation or chemicals. Such easy influence over the semiconducting properties of these materials prompts an investigation of band gap in copper oxides prepared at various pressures, where pressure

is used to create the defects mentioned above. The ability to tune the band gap of materials has been a long sought-after technique in the world of condensed matter physics. Whereas the application to solar power technology is readily apparent, the ability to tune a band gap to emit or absorb specific wavelengths is also applicable to the fields of optoelectronics and computation. Each of these fields require materials with very specific electronic band gaps, particularly when developing laser or LED components.

Our study of the copper(II) oxide (CuO) system is focused on the possibility of increasing the band gap of the naturally occurring CuO. Although the narrow band gap copper(II) oxide is most commonly found in electronic applications as a lithium-doped p-type semiconductor, variations featuring a larger tunable band gap are required for developing applications in optoelectronics and solar cell technology. However, it is still important to note that the ability to freely tune the band gap is not required, just desired. With at least one variant to a material's band gap, some applications can still be considered. For instance, optoelectronics may still benefit if internal reflection at material boundaries can be reduced through carefully designed interfaces. Pairing two materials that are identical except for their band gaps may be an appropriate solution to allow for reduced internal reflection at boundaries while light travels through a device.

Using several samples of CuO prepared at pressures ranging from 0.7 GPa to 8.0 GPa, our study may provide some insight for material synthesis through pressure application. We expect to see a change in band gap as pressure is increased due to the creation of defects produced by the additional pressure to the lattice. Through this investigation, we aim to improve the ability to tune band gaps in transition metal oxides by testing the simple addition of pressure during the synthesis process.

1.2 Molecular Systems

Molecular systems can also be used in novel electronic applications. Some of these systems show promise for being superconducting, whereas others have the potential for showing unique magnetic properties. For this work, we have studied potassium-doped phenanthrene and anthracene as well as Li_2RuO_3, having a similar crystal structure to known hexagonal iridates. Both systems are studied using x-ray absorption spectroscopy to examine the conduction band. X-ray emission spectroscopy is also used to examine the valence band of Li_2RuO_3. Both of these are techniques common to those used in studying the materials discussed above.

1.2.1 Potassium-doped Anthracene and Phenanthrene

With the desire for faster and more efficient computing ever in the minds of researchers, any mention of superconductivity, especially at room temperature, is guaranteed to spark an interest. A theoretical study that brought potassium-doped phenanthrene to light as a potential room-temperature superconductor provided the primary motivation to study this system using XAS in combination with simulations. Phenanthrene and anthracene, two three-ring polycyclic aromatic hydrocarbons, were combined with potassium to create K_3:Phenanthrene and K_3:Anthracene. Previously, systems such as these had not been studied using XAS and theoretical techniques together, making the study a new and novel approach for examining potential superconductor materials as a whole.

1.2.2 Li_2RuO_3

Relative success in the study of the electronic and magnetic properties of hexagonal iridates prompted the study of Li_2RuO_3 which has a similar crystal structure based on $4d$ and $5d$ transition metals. These materials tend to have strongly anisotropic exchange interactions, leading to unusual magnetic properties. However, they can also be viewed as molecular orbital crystals. Molecular orbital crystals have unique physical properties that arise from chemical bonding and the formation of quasimolecular orbitals. These unique properties lead to speculations about a number of different uses in electronic applications, motivating the study of Li_2RuO_3.

1.3 Thesis Organization

The content of this thesis can be split into two main parts. First, introductory concepts and the necessary background will be laid out. Once the basic knowledge has been provided, the focus turns to a discussion of the results for each of the two primary projects and an abbreviated discussion of each of the two secondary projects. In the first portion, one can find the discussion of the physics of transition metals (Chapter 2) along with the descriptions of the experimental techniques and theoretical modelling used to interpret the findings (Chapter 3). It should be noted that the majority of the knowledge in this portion will be derived from literature. The second major element of this work first focuses on the discussion of molybdenum disulphide doped with cobalt (Chapter 4), an example of transition metal impurities introduced into a semiconductor lattice. Next, we include a discussion of a transition metal

oxide, copper(II) oxide, when prepared at varying pressures (Chapter 5). Finally, Chapter 6 offers some discussion of two smaller projects based on molecular system that were studied using the same techniques as the transition metal & semiconductor systems. Overall, the work concentrates on the techniques used to study these materials, motivated by the need for continued development of new materials for electronic applications.

Chapter 2

Transition Metal Properties

> There is no science in this world like physics. Nothing comes close to the precision with which physics enables you to understand the world around you.
>
> – NEIL DEGRASSE TYSON

The work for this thesis relies heavily on transition metals and the properties unique to them. In this chapter, we focus on elements from the *d-block* in the periodic table – more specifically, the top row of these elements – and discuss the necessary background information for understanding these properties as they apply to condensed matter physics. These elements are often referred to as $3d$ transition metals, named for the the $3d$ electrons occupying the valence shell in each of these elements. First, we discuss in more depth what we mean by $3d$ transition metals and follow by introducing the behaviour of $3d$ electrons. An introduction of correlation effects and the resulting physics will follow. Finally, we examine the electronic structure formed by these $3d$ electrons and follow with a brief review of the

band gaps in transition metal solids, including how they apply to condensed matter physics.

2.1 Radial Wavefunctions and Localized $3d$ Electrons

We begin with a brief discussion of the outer electrons in transition metals. In the *d-block* of the periodic table, elements typically have an unfilled valence shell containing only $3d$ electrons, hence the name $3d$ transition metals. For example, isolated cobalt has a configuration of $[\mathrm{Ar}]3d^7 4s^2$. Although it seems that the outermost shell must be the $4s$ orbital, the $3d$ orbital actually extends farther from the nucleus, a concept that will be discussed below. With a valence configuration of $3d^7$, only the d-electrons contribute to cobalt's properties because it is these valence electrons that lead to the unique properties of materials.

Quantum mechanics provides the basis for our understanding of transition metal properties. It was not until quantum mechanics was developed that we had a theoretical explanation of shells and orbitals, despite the early recognition of groups and trends in the periodic table. The Schrödinger equation (Equation 2.1) provides the basis for solving the wavefunctions for any atom or group of atoms. Although we can always make an approximate solution for Schrödinger's equation, only the hydrogen-like atom, the case of one electron and one proton, has an analytic solution.

$$\hat{H}\psi(r,\theta,\phi) = E\psi(r,\theta,\phi) \tag{2.1}$$

In the time-independent Schrödinger equation above, $\hat{H}$ is the Hamiltonian operator representing the system, ψ is the wavefunction solution (represented in spherical coordinates) and E is the energy of the system.

Given that it is the only analytical solution, we first study the hydrogen-like system

before building up to the many-electron systems of transition metals. Equation 2.2 shows the Hamiltonian that represents the single electron and single proton system where $\mu = \frac{m_e m_p}{m_e + m_p}$. By inserting the Hamiltonian into Equation 2.1, we get Equation 2.3, which can be solved by separating the radial, polar, and azimuthal parts, and solving each part individually. Once the solutions are brought back together (shown in Equation 2.4a), the hydrogen atom solution for the electron wavefunction can be spit into radial ($R_{n,\ell}(r)$) and angular ($Y_{\ell,m}(\theta,\phi)$) parts described by the quantum numbers n, ℓ, and m, as seen in eq. 2.4b.

$$\hat{H} = -\frac{\hbar^2}{2\mu}\nabla^2 - \frac{e^2}{4\pi\epsilon_0 r} \tag{2.2}$$

$$-\frac{\hbar^2}{2\mu}\left[\frac{1}{r^2}\frac{\partial}{\partial r}\left(r^2\frac{\partial\psi}{\partial r}\right) + \frac{1}{r^2\sin\theta}\frac{\partial}{\partial\theta}\left(\sin\theta\frac{\partial\psi}{\partial\theta}\right) + \frac{1}{r^2\sin^2\theta}\frac{\partial^2\psi}{\partial\phi^2}\right] - \frac{e^2}{4\pi\epsilon_0 r} = E\psi \tag{2.3}$$

$$\psi = R(r)\Theta(\theta)\Phi(\phi) \tag{2.4a}$$

$$= R_{n,\ell}(r)Y_{\ell,m}(\theta,\phi) \tag{2.4b}$$

Recall that quantum numbers represent aspects of electron behaviour, where n is closely tied to the energy of the electron and corresponds to the electron shell number in the electron configuration. Next, ℓ represents angular momentum, and its value, $\ell = 0, 1, 2, \ldots$, corresponds to the $s, p, d, \ldots$ orbitals. Finally, m is tied to electron spin, which will not be discussed here.

When we plot the radial portion of the hydrogen wavefunction (Figure 2.1), we note the presence of nodes for many combinations of n and ℓ. Note also that the number of nodes

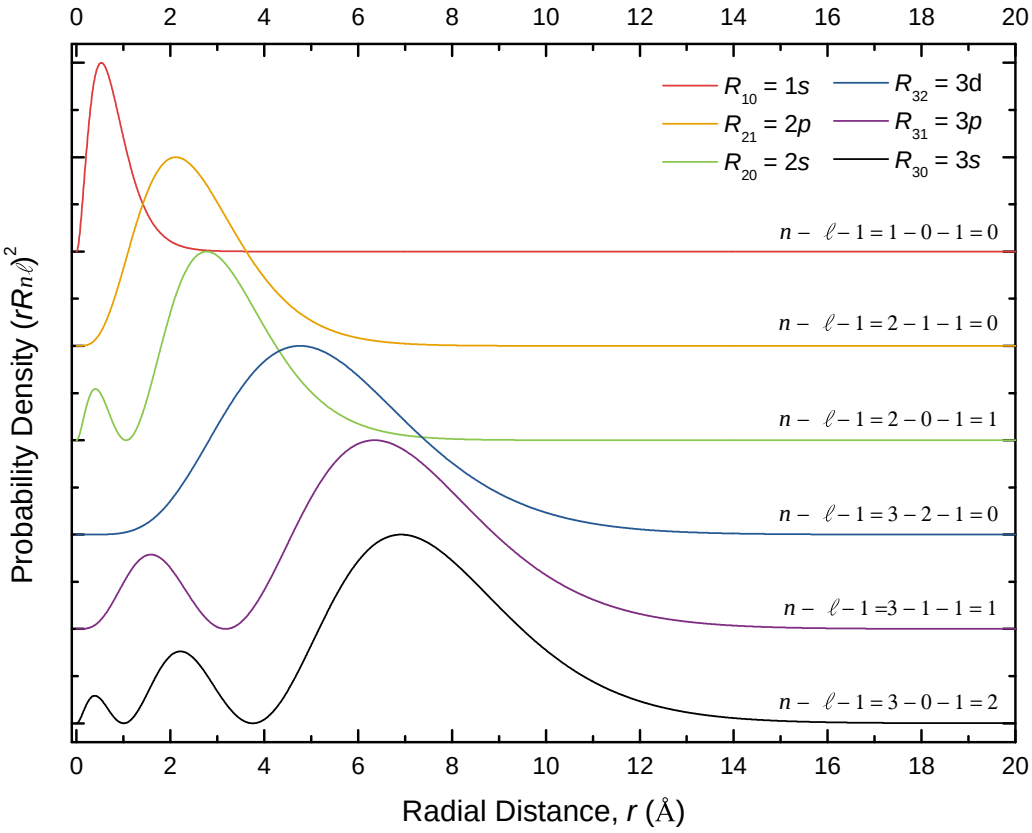

Figure 2.1: Radial wavefunctions for different quantum number configurations in the hydrogen-like atom. Those wavefunctions with nodes are those most loosely bound, while the configurations with no nodes are most tightly bound to the core.

is proportional to the spreading of the wavefunction. Wavefunctions with more nodes reach larger values of r. The number of nodes is given by $n - \ell - 1$. For $3d$ electrons where $n = 3$ and $\ell = 2$, there are no nodes present, resulting in the most tightly bound electrons. These closely held $3d$ electrons experience localization, an important property for understanding and isolating the behaviour of valence electrons in $3d$ transition metals.

If we consider each electron in a transition metal to behave radially like the hydrogen electron, we begin to understand how the different shells of electrons behave. Consider that since the $4s$ electrons have three nodes, ($n = 4$ and $\ell = 0$) they extend much farther from

the core than the $3d$ electrons and are thus stripped first during oxidization. Additionally, localization is also encouraged by the core electrons that are able to repel the valence electrons of neighbouring atoms. This repulsion weakens the bonds between the $3d$ elections and neighbouring atoms, further localizing the $3d$ electrons causing them to behave as if the atom they belong to is isolated.

The tightly bound localized $3d$ electrons are isolated from the rest of the electrons due to the reasons discussed above, and as such, they can be described by a wavefunction that is almost entirely radial. However, it is important to keep in mind that the angular behaviour of the wavefunction is still part of the solution and plays an important role when discussing crystal fields and bonding in solids. Crystal fields as they appear in solids will be discussed further in Section 3.6.

2.2 Electron Correlation and Multiplet Physics

The localization discussed above leads to strong interaction between the $3d$ electrons known as electron correlation. Simply put, electron correlation is the phenomenon of collective behaviour in electrons. In systems with strong electron correlation, the perturbation of one electron leads to all other electrons experiencing the same effect without having been probed directly.

We begin by considering the simplest case, that of an isolated atom. Although this is not entirely realistic, it provides a a good starting point before examining electron behaviour in solids in Section 2.3. Considering only the $3d$ electrons knowing they are responsible for interactions, an isolated atom will have many different ways to arrange those $3d$ electrons

within the orbital, each arrangement corresponding to an eigenstate otherwise known as a *multiplet*. Some of these multiplets will be non-degenerate – each having unique energies – but many can be degenerate.

Across the top row of the *d-block*, the number of multiplets and their energies are extremely sensitive to the number of d electrons. Their sensitivity to the local bonding environment and atomic number will be discussed in Section 3.1.1, but is important to note here while discussing multiplets. We can learn much about a transition metal compound by probing the multiplet states, given the sensitivity to the number of d electrons, local bonding environment, and atomic number. Although a variety of techniques can be used to accomplish this goal, this work focuses on the use of x-ray absorption and x-ray scattering.

As mentioned above, the atomic point of view is not physically realistic. However, $3d$ transition metals can be explored by studying multiplets once we consider multiplet behaviour in solids. Next we discuss these interactions as they apply to the case of a solid as opposed to the atomic view.

2.3 Electronic Structure and Band Gaps

After it was realized that the first iterations of band theory could not explain the insulating behaviour of transition metal oxides, several theories were developed that can explain the different types of band gaps in transition metal solids. One of the first theories was developed by Mott [19–21] and Hubbard [22,23], who reasoned that electrons would experience coulomb repulsion as they travelled through the solid, which required more energy than band theory considered. The energy cost for electron hopping from one site to another is given as U.

This theory describes the Mott Hubbard (MH) band gap. Alternatively, when electrons hop from ligand sites to metal sites giving rise to the Charge Transfer (CT) bands, the associated energy is given as Δ. Given that the two theories are somewhat opposed to one another, it is the smaller value of U and Δ that determines which phenomenon defines the band gap, which will be explained further below.

When we examine the Density of States (DOS) of a transition metal solid, we see hybridization due to the bonding of metals with ligands. This mixed state manifests as a weak character coincident with a strong character (i.e., weak ligand character with strong metal character). Each band gap type shows some ligand character in both the valence band (VB) and the conduction band (CB), allowing us to use the mixed character in the DOS to understand how U and Δ arise.

The two theories discussed above can be examined individually to understand how the two interact. In the Mott Hubbard type, both the top of the VB and the bottom of the CB are dominated by metal sites as opposed to ligand sites. This leads to the band gap being directly related to U, the energy associated with hopping between metal sites. Conversely, a charge transfer solid has a large U that pushes the metal states to the bottom of the VB, leaving the top of the VB to have mostly ligand character. Since the conduction band remains unchanged, we now have a band gap defined by the jump between ligand and metal sites, which is related to Δ. It is clear now that while U and Δ are properties of both types of band gaps, U determines how deep the metal sites sit in the VB DOS. Consequently, the relative strengths of U and Δ are most important in determining which phenomenon dominates the material. Through a simple evaluation of which value is greater, the type of band gap can be identified.

As it applies to the material studied in this project, we can take advantage of the hybridization present in these materials. Hybridization leads to the presence of ligand character (either weak or strong) at the top of the valence band and the bottom of the conduction band. Knowing that there is ligand character in both bands, we can probe the edges corresponding to the ligand to experimentally determine the band gap of these materials. These experimental techniques will be discussed further in Section 3.1.2.

Chapter 3

Experimental Probes and Applicable Modelling

I can only speak for particle physics. But it has become obvious that on the experimental side, there has been a huge evolution in the number of people who have to collaborate because of the gigantic size of the instruments used, but also because of the enormous task that is data analysis.

– PETER HIGGS

In this chapter, we discuss the experimental and theoretical techniques used to analyse the chosen materials. The entirety of the work is centred around the concept of performing experiments and using modelling as a way to understand the experimental outcome. We focus our interest on the electronic structure of these materials, a property that can be probed through the use of synchrotron radiation. Although there are a large number of techniques that can be used, we primarily employ those valuable to condensed matter physics and the

study of materials with $3d$ electrons. These techniques include x-ray absorption spectroscopy, x-ray emission spectroscopy, and resonant inelastic x-ray scattering, all of which will be described below. In addition to a discussion of these techniques, we also briefly introduce the synchrotron sources where these experiments are performed. Finally, a discussion of the modelling used for analysis will be presented.

3.1 X-Ray Absorption Spectroscopy

X-Ray Absorption Spectroscopy (XAS) is one of the most commonly used techniques for probing element-specific characteristics. Typical experiments scan over a range of incident photon energies corresponding to a particular absorption edge. The absorption of the photons can be monitored, and the energy-dependence can be determined. Near the absorption edge, a number of different processes can occur when a photon is absorbed by a material. When the energy matches the absorption threshold, the absorption is dominated by the process where core electrons are excited into bound states [24], as depicted in Figure 3.1 a). The fine structure of these excitations is material and site dependent and may fall anywhere within a wide range of excitations – including the excitations of electrons, phonons, plasmons, etc. These excitations are representative of the unoccupied Density of States (DOS), and as such, x-ray absorption techniques provide an indirect probe for the conduction band. Specifically, XAS probes particular electron shells (s, p, d, etc.), providing the partial Density of States (pDOS), unlike photoelectron spectroscopy, which probes the total DOS. As such, x-ray absorption techniques provide an indirect probe for the conduction band. At higher excitation energies, core electrons are given sufficient energy to escape to the continuum resulting in a

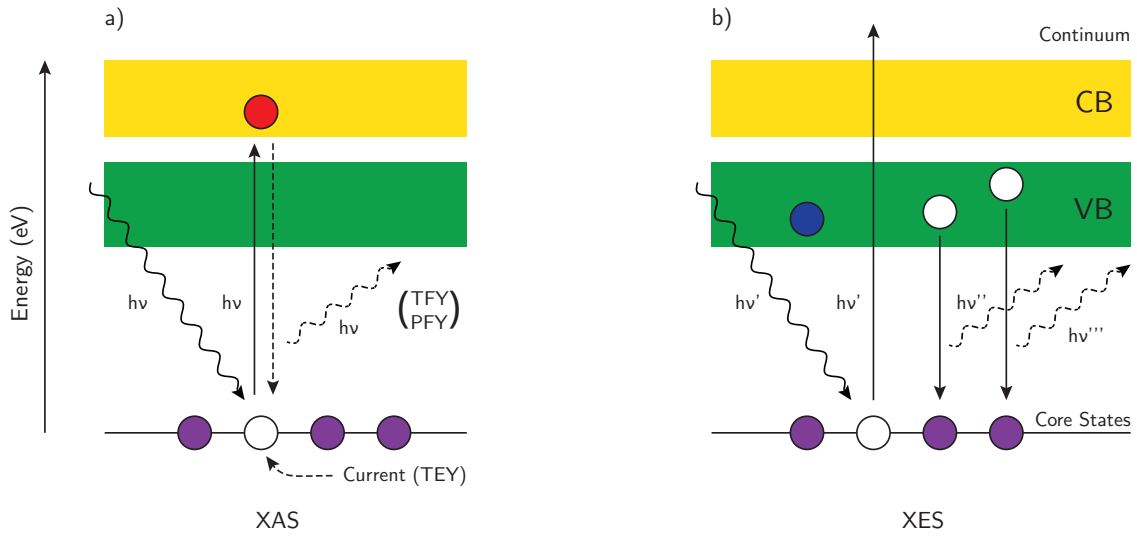

Figure 3.1: Illustration of the XAS and XES processes. Figure a) shows the x-ray absorption process where a photon is absorbed by a core electron and the electron is subsequently excited into the conduction band. Figure b) shows the x-ray emission process where decay from the valence band to empty core states produces detectable photon emission.

trend of decreasing absorption intensities. For this work, we are most interested in the Near Edge X-Ray Absorption Fine Structure (NEXAFS) [24] with energies close to the binding energies of the corresponding edge. In this NEXAFS region, one can probe the fine structure near the onset of the unoccupied DOS.

Before discussing XAS as it behaves for different element-specific edges, it is important to examine the need for probing a variety of edges in the first place. While the aforementioned unoccupied DOS is a ground state property, XAS is derived from an excited state that includes effects attributed to the presence of core holes. Most often, the core hole results in the XAS shifting to higher energies, giving rise to error when determining the band gap from XAS and XES. On a more positive note, despite its universality, the core hole effect does vary in strength depending on the edge being probed. Typically, the core hole effect is much

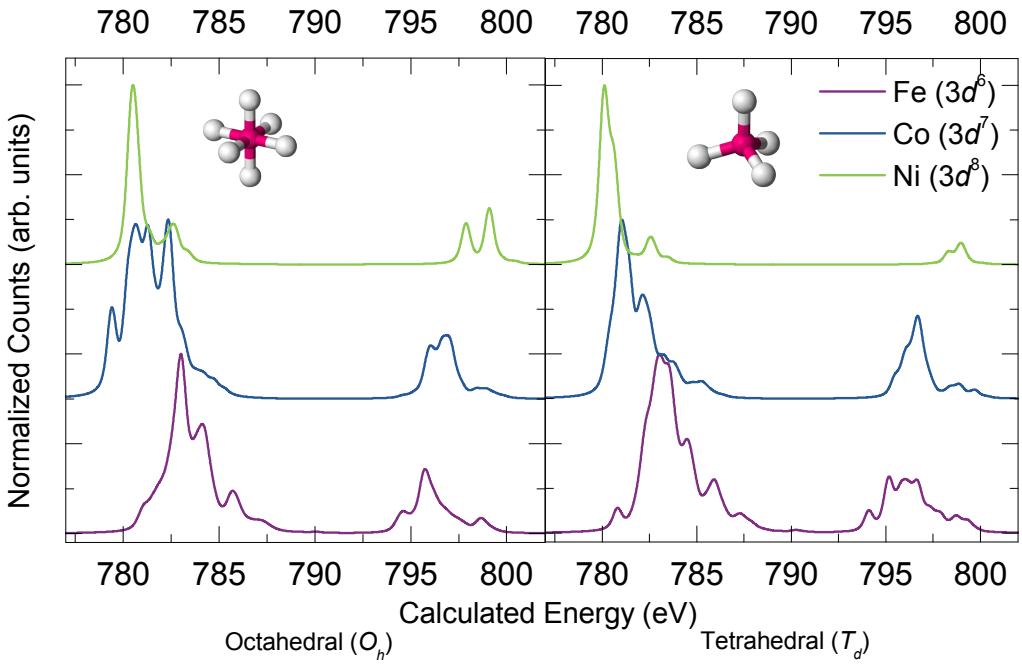

Figure 3.2: $L_{2,3}$ XAS for a number of different transition metals with different local environments. The left panel shows the calculated spectra for three transition metals in octahedral coordination, while the right panel displays the same metals in a tetrahedral environment.

stronger in transition metals, but comparably weaker in lower Z elements such as oxygen, sulphur, and nitrogen. Armed with this knowledge, we can carefully choose the edges to probe when we want band gap information as opposed to information on the local bonding environment.

3.1.1 XAS of Transition Metal $L_{2,3}$ Edges

In studying metal $L_{2,3}$ edges, we consider only the $2p \rightarrow 3d$ excitations since it has been shown that the excitations into the $3d$ orbitals dominate those into the $4s$ orbitals [25]. $3d$ electrons of transition metals tend to remain localized [26], causing a strong overlap between the $2p$ wavefunction of an unpaired electron and the $3d$ valence wavefunction. Interactions

between individual $3d$ electrons and the strong wavefunction overlap lead to spectra dominated by multiplet effects [27]. When such spectra are dominated by multiplet effects, the general shape depends largely on the number of d electrons present [26]. If we look closely at Figure 3.2, a set of calculated spectra for metals with different numbers of d electrons and with different local bonding environments, we can see how the spectra change with those parameters. The L_2 and L_3 peaks shift farther apart with an increasing number of d electrons, and the fine structure changes from the octahedral bonding (left) to tetrahedral bonding (right).

Another key feature of $L_{2,3}$ XAS is that different local environments around the absorbing site produce significantly differing spectral shapes. For instance, octahedral and tetrahedral bonding coordination will produce different spectral shapes. In this manner, we can usually make a very accurate prediction at the coordination of an atom from only the XAS.

Finally, the spin-orbit splitting of the L_2 and L_3 peaks, resulting from the energy difference between the $s = {}^1\!/_2$ and $s = {}^{-1}\!/_2$ spins, is proportional to the binding energies, leading to different edge onset energies for different elements [28]. This proportionality is simply a product of the Coulomb effect, where larger groups of electrons will experience greater repulsion from one another. The splitting phenomenon leads to spectra being element specific, so long as the constituent elements have binding energies that can be differentiated.

These three key observations regarding transition metal XAS can be applied to the materials studied in this work. One can study the valency of the transition metal and the local bonding environment via the spectral shape, and one can be certain to be element selective knowing that the peak splitting is dependent on the element-specific binding energy. It is also important to note that element specificity is a great advantage for probing the low

concentration of DMS dopant atoms due to its independence from the amount of dopant present.

3.1.2 XAS of Complimentary Edges

Recall from Section 2.3 the discussion of probing the ligand edges to determine the band gap of transition metal oxides. Similarly, we use the combined XAS and XES of complimentary edges to determine the band gap for other transition metal semiconductors and insulators. We examine the complimentary edge primarily due to the strong influence of the core holes in any transition metal $L_{2,3}$ spectra. As such, probing the $L_{2,3}$ edge will not show a true band gap. Instead, we probe the band gap using a complimentary edge in the same fashion as we would transition metal oxides.

If we examine Figure 3.3, we see an example of how the band gap is determined through XAS and XES spectra taken at the same edge. Below, in Section 3.2, you will find a detailed discussion of the XES technique. In determining the band gap, we choose the valence band maximum from the XES to represent the bottom of the band gap and the conduction band minimum from the XAS to represent the top of the band gap. These values are determined in a variety of ways, often depending on the shape of the spectra. When sharp features are present in the NEXAFS, we can use the second derivative method to choose these values, which is shown in the lower panel of Figure 3.3. Conversely, a flat feature may require methods that consider the slope of the spectra near the edge. The difference between the two chosen energies gives the band gap value.

While on the topic of band gap determination, it is prudent to elaborate on the two methods for determining band gap and their use. Both methods have a place in analysis,

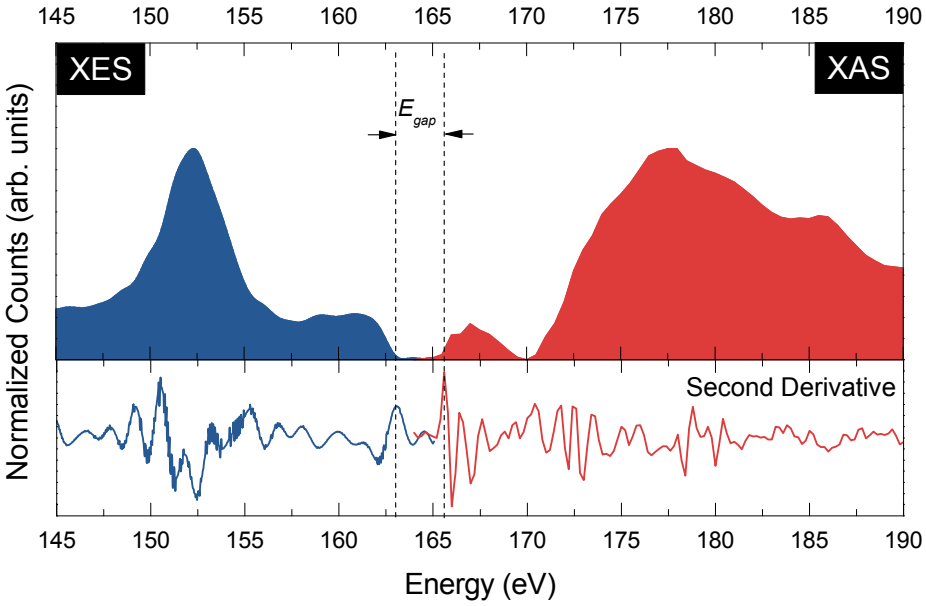

Figure 3.3: Example of an experimental band gap for ZnS at the S $L_{2,3}$ edge. We use complimentary XAS and XES data to determine the valence band maximum and conduction band minimum, whose difference is equal to the band gap. Typically, these values are determined using second derivatives (shown above).

but the choice of method often depends on the shape of the spectrum. The second derivative method, while better defined, requires a steep slope at the onset of the band gap. Once the second derivatives are calculated and plotted, the first *reasonable* peak in the second derivative indicates the onset of the band gap. We say reasonable because some features in the second derivative clearly do not correspond to the edge, which can be seen in Figure 3.3 around 164 eV where a small peak with no corresponding XES feature appears in the second derivative. Conversely, the linear extrapolation method is used when the slope at the onset is shallow. Two best fit lines are used, one through the onset slope and one through the background, and their intersection represents the onset of the band gap. Although either method can be used since the difference between the two is typically much smaller than the error in the data, the second derivative method is often preferred because it is less ambiguous.

3.2 Nonresonant X-Ray Emission

A standalone or complimentary technique to XAS, X-Ray Emission Spectroscopy (XES) measures the photons emitted as valence electrons decay to fill an excited core hole. We use two types of XES for characterizing materials, Non-resonant X-Ray Emission Spectroscopy (NXES) [29] and Resonant Inelastic X-Ray Scattering (RIXS) [30, 31]. The two can be used together, whereby the resonantly excited RIXS is used to calibrate the NXES, allowing for XAS, NXES, and RIXS spectra to be internally consistent with one another. However, RIXS alone still provides valuable information and will be discussed below.

When electrons are excited at energies well above the absorption threshold, the decay of electrons into the core holes produces a spectrum that closely approximates the occupied partial DOS of the corresponding edge. Consequently, these spectra provide a probe of the valence band. Figure 3.1 b) provides an illustration of the NXES process where incident photons create core holes that are then filled by electrons decaying from the valence band. The photons given off by this decay process are of varying energies and their number depends on the valence band density of states. Examination of the NXES allows for the determination of the valence band maximum energy. Thus, when combining the XAS and NXES at the edges of constituent materials other than the transition metal, we can approximate the experimental band gap for the bulk material. Typically, the second derivative method is employed to determine the upper end of the valence band (corresponding to the valence band maximum) and the beginning of the conduction band (conduction band minimum).

3.3 Resonant Inelastic X-Ray Scattering

RIXS forms somewhat of a hybrid between XAS and NXES. Monochromatic x-rays are used to excite core electrons into unoccupied states, a process similar to XAS, but like NXES, energy resolved x-rays are given off after subsequent decay. What separates RIXS from NXES is that NXES induces ionization of atoms, whereas RIXS appears as "charge neutral" excitation of atoms. In RIXS, the material is excited at resonant energies and inelastic scattering is responsible for the x-rays detected.

The RIXS process is coherent and performed in a single step. To put it more simply, the electrons in the system are scattered from an initial ground state to an excited final state through virtual intermediate states that have been enhanced by the resonant energy. The scattered electron wavefunctions experience interference with one another as they "travel" to the final state. As such, the coherent sum includes the interference effects acting on the wavefunctions. An analogue to this process is the interference pattern created when light passes through an array of slits. Figure 3.4 shows the two processes and how their initial, intermediate, and final states are related. Of course this simplistic analogue appears as as two-step process. However, just as the multi-slit experiment cannot be broken down to observe individual photons, the RIXS process cannot be separated to identify the enhanced XAS states.

It's important to note that in $L_{2,3}$ RIXS, the intermediate states are exactly the $L_{2,3}$ XAS final states. This provides us with two important tools: we can calculate RIXS from calculated XAS; and we can obtain different RIXS measurements for each incident energy. Thus, by scanning over incident energies, we can enhance the those intermediate XAS states

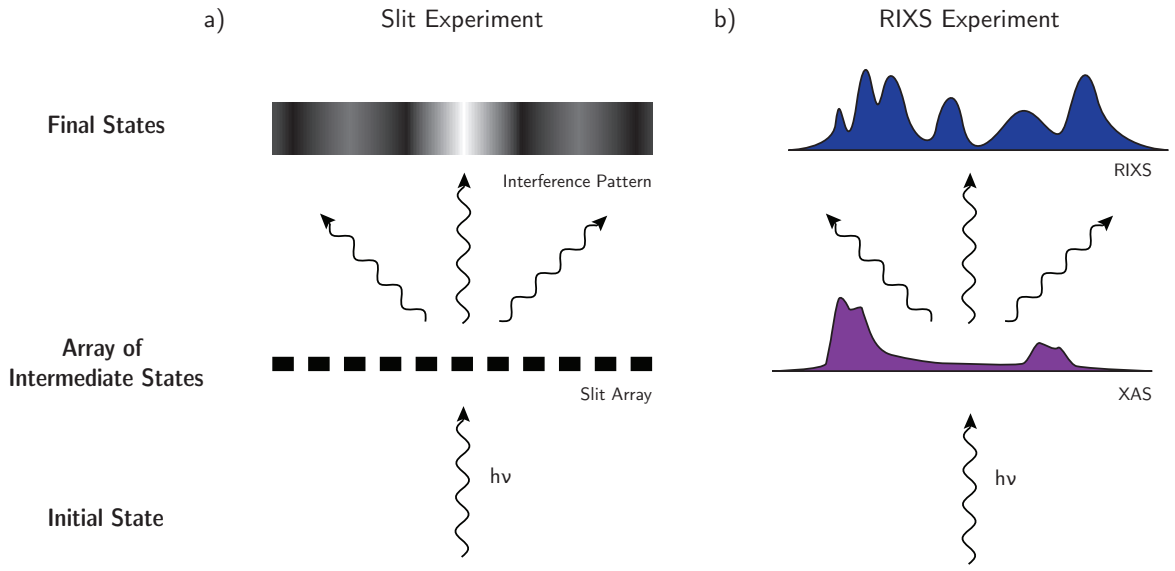

Figure 3.4: Illustration of the RIXS process. Panel a) shows the resulting interference once light is passed through an array of slits. Using a direct analogue, panel b) shows how the RIXS experiment for the $L_{2,3}$ edge is a result of a photon scatting through the intermediate state, the $L_{2,3}$ XAS.

each in turn, in order to gather information on the different excitations that contribute to a RIXS spectrum. Because the RIXS process allows for the system to remain in an excited state after decay, the final state can have rearranged electronic occupations of orbitals, electrons that have hopped to different bands, or other manifestations of the excited state, each of which arise as an excitation in a RIXS spectrum.

Whereas NXES is most often used in the determination of experimental band gap, RIXS can be utilized to probe the local environment of the ion and evaluate the band gaps in charge transfer semiconductors and insulators. Typically, a wider charge transfer band in the RIXS measurement will correspond to a wider NXES band. The same trend holds for narrower bands. For example, a RIXS measurement with a wider charge transfer band than another corresponds to a wider NXES where the valence band maximum is higher and, consequently,

band gap is smaller. The opposite would be true for the RIXS with the narrower charge transfer region. With this information, one can make a qualitative statement about the size of the band gap with respect to another reference material using only RIXS measurements.

3.4 Detection Techniques

The following sections introduce the technical aspect of how the above experiments are performed and some of the specific techniques that can be performed at the synchrotron sources where data was acquired for this work.

3.4.1 Detection of XAS

At the most basic level, x-ray absorption detection relies on the concept that at a particular energy, the number of states available in the conduction band will determine how efficiently electrons can be excited from the core level. Under the important assumption that these states and core holes are in abundance, we can roughly relate the number of photons absorbed to the number of states available. Equation 3.1 relates the transition probability from an the initial to final state ($T_{i\rightarrow f}$) to the final DOS (ρ_f) through a constant factor and the transition matrix element. Thus, we have a direct relationship between the measured absorption and the conduction band density of states. The transition matrix element determines how closely $T_{i\rightarrow f}$ represents the conduction band DOS. If the transition matrix element is heavily influenced by multiplet effects or other excitations, $T_{i\rightarrow f}$ is less representative of the DOS, whereas if the transition matrix element is nearly constant, $T_{i\rightarrow f}$ is nearly identical to the conduction band DOS.

$$T_{i\to f} = \frac{2\pi}{\hbar} \left|\langle \Psi_f | H' | \Psi_i \rangle\right|^2 \rho_f \tag{3.1}$$

If we again consider panel a) of Figure 3.1, we can see a simplified schematic of the XAS process, including the two primary mechanisms that allow for detection. To start the XAS process, an incoming photon excites a core electron into an empty state in the CB. The now highly excited electron can decay through a few mechanisms that when detected are known as *yield techniques*, two of which will be discussed below.

The first commonly used yield technique is known as total electron yield (TEY). From the excited state, decay occurs through the giving off of electrons (electrons produced in this manner are known as *Auger* electrons). As these Auger electrons are created, they are allowed to travel out of the sample via scattering while new electrons are supplied to replenish those excited out of the core, creating a current than can be measured (Figure 3.1 a)). The current is directly proportional to the number of core holes created, which in turn is proportional to the CB partial DOS. Recall that electrons have a smaller escape depth than the photons probing the material. Consequently, TEY probes only the first few nanometres of the sample because it depends on the Auger electrons travelling out of the sample once they have been created. As a result, TEY is referred to as a surface sensitive technique.

Alternatively, excited electrons in the CB can also decay back into the core holes by emitting a photon. Since any electron in the CB is a product of excitation by x-rays, they have an energy equivalent to the current beamline energy and will thus emit a photon with the same energy in order to decay back to the core, resulting in an elastic peak. If all present photons are detected, including lower energy photons from secondary processes as well as those from

the elastic peak, the technique is referred to as total fluorescence yield (TFY). Conversely, if only photons in a specified energy range are detected, the technique is known as partial fluorescence yield (PFY). Using either method, we can relate the number of photons to the number of x-rays absorbed at a particular energy. Whereas TFY produces low energy fluorescence photons in abundance (as opposed to far fewer high energy photons), only collecting photons over the region of interest gives fewer overall photons detected. Consequently, a truer signal will be measured for PFY where we filter out photons from secondary processes not directly related to the absorption process. However, to have enough photons for PFY to have strong statistics, count times must be increased drastically, making PFY a less appealing option when time is limited. In these processes, the emitted photons typically travel much larger distances than emitted electrons, resulting in TFY and PFY having much larger probing depths than TEY.

3.4.2 Detection of NXES and RIXS

Knowing how the emission process takes place, we can now address how it is detected. Recall that we can probe the valence band by exciting electrons out of the material and into the continuum, a process that creates core holes. Electrons decay into those core holes, giving off photons with energies dependent on their location in the VB. While RIXS experiments on the inelastic scattering of x-rays rather than the decay and subsequent photon emission seen in XES, we can still detect the photons from both mechanisms using the same detection method.

During a measurement, all photons given off from a sample are collected in an energy resolved manner using an area sensitive detector. Before the NXES or RIXS spectrum can be

extracted, the 2-dimensional data must have its curvature corrected, an artifact that arises due to the diffraction geometry. After correction, the pixels are summed over each column and calibrated to an eV scale, resulting in the overall spectrum. It is important to also note that although the same detection technique is used for both NXES and RIXS, a much higher resolution is required to resolve RIXS features than NXES. For this reason, not all beamlines that provide NXES detection can also provide highly resolved RIXS, limiting the beamlines at which these measurements can be taken.

3.5 Experimental Facilities

Now that we have a good idea of how experiments are performed, we will give a brief introduction of the facilities where the data in Chapters 4 and 5 was taken. We focus specifically on the REIXS beamline at the Canadian Light Source (CLS) and Beamline 8.0.1 at the Advanced Light Source (ALS).

3.5.1 REIXS Beamline at the Canadian Light Source

The Resonant Elastic and Inelastic X-ray Scattering (REIXS) beamline was constructed by the Moewes group at the University of Saskatchewan to provide high quality condensed matter data. Although its primary uses focus on the XAS, NXES, RIXS, and MXCD (magnetic x-ray circular dichroism) techniques performed on one leg of the beamline, a second leg provides resonant soft x-ray scattering (RSXS) in addition to the XAS and MXCD techniques. For this work, we focus on the XES endstation, which is shown schematically in Figure 3.5. It should be noted that two beamline components are included but not used – both of these

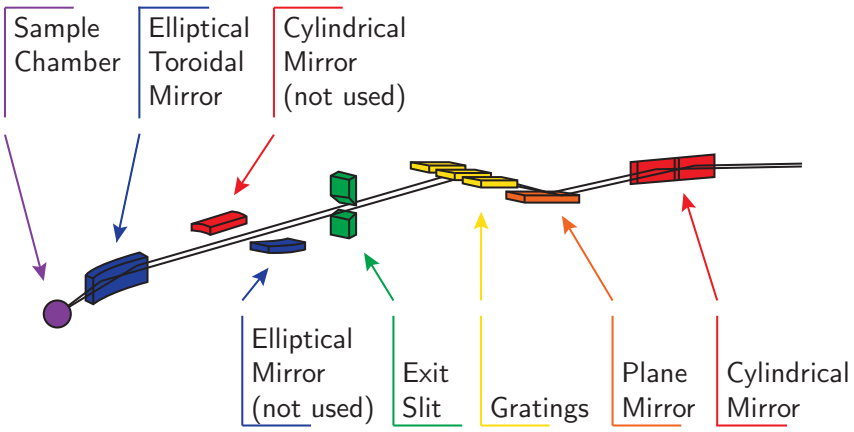

Figure 3.5: Schematic of the REIXS beamline optics. After passing through a series of mirrors, gratings, and the exit slit, x-rays are directed into the XES endstation by removing the cylindrical and elliptical mirrors that serve to direct the beam into a secondary endstation. Figure adapted from REIXS documentation [32].

are used to direct the beam to the second endstation.

The XES endstation is built for producing high quality condensed matter data. An elliptically polarized undulator provides an energy range of 80 – 2000 eV. At $E = 100$ eV, the beamline has resolving power ($E/\Delta E$) of 20000 and a resolving power of ≈7700 at $E = 1000$ eV. The number of photons incident on the sample per second (flux) is 1 x 10^{12} and 5 x 10^{11} at 100 eV and 1000 eV, respectively. Each of the many possible polarizations – linear in any direction, left and right circular, and elliptical – have nearly the above resolving power and flux capabilities while maintaining a spot size of 60 x 10 μm.

3.5.2 Beamline 8.0.1 at the Advanced Light Source

Beamline 8.0.1 (BL8) at the Advanced Light Source (ALS) provides resources for both XAS and XES measurements. Its strengths include high resolution, linearly polarized light and its x-ray fluorescence spectrometer with a Rowland-circle type grating. BL8 operates at

energies ranging from 80 eV to 1250 eV, providing coverage for all $L_{2,3}$ edges of the $3d$ transition metals. Although BL8 provides the same functionality as the REIXS beamline, it still serves an important role in providing high resolution $3d$ transition metal RIXS.

3.6 Multiplet Calculations

The aforementioned calculations will be performed using code developed by Robert Green [26] and based on the publicly available multiplet code by Thole *et. al.* [33]. This program allows for both XAS and RIXS simulations using a number of possible models. In the case of L edge transition metals, local effects dominate the spectra; therefore, only atomic eigenstates are required to perform the calculations. As a result, the wavefunctions are first determined for ground and excited states, and then those wavefunctions are used to calculate the required transitions. When calculating both XAS and RIXS, the program makes use of the Kramers-Heisenberg formula

$$\frac{d^2\sigma}{d\Omega_{k'}d(\hbar\omega'_k)} = \frac{\omega'_k}{\omega k}\sum_{|f\rangle}\left|\sum_{|n\rangle}\frac{\langle f|T^\dagger|n\rangle\langle n|T|i\rangle}{E_i - E_n + \hbar\omega_k + i\frac{\Gamma_n}{2}}\right|^2 \delta(E_i - E_f + \hbar\omega_k - \hbar\omega'_k) \qquad (3.2)$$

where $\hbar\omega'_k$ is the energy of the emitted photons, $\hbar\omega_k$ is the energy of the incident photons, $d\Omega_{k'}$ is the solid angle centred in the k' direction, T is the transition operator, and Γ_n is the intrinsic linewidth of the intermediate state. $|i\rangle$, $|n\rangle$, and $|f\rangle$ are the initial (ground), intermediate, and final states of the system with energy E_i, E_n, and E_f, respectively. Equation 3.2 only shows the first coherent term in the Kramers-Heisenberg equation, the only term used in the calculations presented here. It is an expression for the cross section of photon scattering

after interaction with an electronic system (a more in-depth discussion can be found in references [34–36]).

There are four possible models used in calculating the transitions: the atomic model, the crystal field model, the ligand field (cluster) model, and the impurity model. The four models are listed from least complex to most complex, beginning with simple atomic Hamiltonians and increasing to complex bands of charge transfer configurations.

After examining the model descriptions below, it becomes clear that one can use the multiplet calculations to simulate experimental spectra of transition metals with spectra dominated by $3d$ electron transitions. The model which matches best not only gives information about the interactions of the system, but in the case of crystal field, cluster, and impurity models, can also provide a powerful tool for determining the local bonding environment. For instance, in the Co:MoS_2 system, one can determine how the cobalt atoms have been incorporated into the host lattice. Positioning possibilities include direct lattice substitution, interstitial doping where the atoms reside between crystal planes, and the formation of clusters.

Theory tell us that in order to describe any electronic system, we must solve Schrödinger's equation. However, there is no analytical solution if more than one atom is present in the system. Consequently, iterative approaches have been developed for studying these systems. Below we present some of the iterative "solutions" necessary for recreating spectra of transition metals.

3.6.1 Atomic Model

As its name suggests, the atomic model considers only the interactions between the nuclei and electrons of nearest neighbours. Its simple Hamiltonian consists of only electron-nucleus, electron-electron, and spin-orbit interactions as shown in Equation 3.3.

$$H_{atom} = H_k + H_{n-e} + H_{e-e} + H_{so} \tag{3.3}$$

$$= -\frac{\hbar^2}{2m}\sum_i \nabla_i^2 - \sum_i \frac{Ze^2}{r_i} + \sum_{i<j}\sum \frac{e^2}{r_{ij}} + \sum_i \xi_i(r_i)(\mathbf{l}_i \cdot \mathbf{s}_i) \tag{3.4}$$

The four Hamiltonians in Equation 3.3 represent electron kinetic energy, electron-nucleus interactions, electron-electron interactions, and electron spin-orbit interactions. The summation indices are over all electrons in the system while r_i represents the distance from the nucleus (taken at the origin) to the i-th electron and r_{ij} the distance between electrons i and j. The operators $\mathbf{l}_i$ and $\mathbf{s}_i$ are the orbital and spin angular momentum operators, respectively, and ξ_i is a proportionality factor. Here the equation for H_{so}, which is used in the calculations presented, represents one possible simplification using only one particular set of assumptions commonly used for the atomic model.

Once the iterative solution has been found, interactions between electrons appear as integrals, often called Slater integrals [28]. We use κ to represent the scaling of the Slater integrals, and they can be described through energy parameters that define intra-atomic Coulomb and exchange interactions between electrons. The Slater integrals are the primary parameters used in the atomic model. It should be noted that often some reduction of the integrals is needed for the calculation to match experimental spectra, which is achieved

through the scaling factor mentioned above.

Although not typically accurate for any condensed matter systems, the atomic model's ability to describe isolated atoms makes it a powerful tool for rare-earth compounds [37, 38] due to the highly localized nature of the $4f$ electrons.

3.6.2 Crystal Field Model

Crystal field calculations are adapted from the atomic model by including crystal fields. The concept, described by Bethe [39] in 1929, simulates neighbouring atoms as point charges so that the atom of interest is only subject to electrostatic potential (shown in Equation 3.5) in addition to the potentials already considered in the atomic model. These "crystal fields" then lead to the splitting of the energy levels of the atom of interest. The resulting energy levels are highly dependent on the local symmetry. The addition of a crystal field potential term to the Hamiltonian is the only difference between the atomic and crystal field models.

$$H_{CFM} = H_{atom} - eV(\mathbf{r}) \tag{3.5}$$

When we discuss energy splitting for an atom with $3d$ electrons, we begin with the most general atomic coordination and then move to more complex systems. In the spherical system, which has the highest local symmetry, the $3d$ orbitals are all degenerate. The energies of the $3d$ orbitals split as soon as the local symmetry is reduced. For instance, in octahedral (O_h) coordination, the orbitals split into two different energy levels – the higher known as e_g and the lower as t_{2g}. The difference between the two energy levels is given as $10Dq$, the key parameter in crystal field calculations. In tetrahedral (T_d) coordination the orbitals split

into the same e and t_2 levels as O_h but the splitting is reversed. Here the g subscripts are removed because there is no inversion symmetry in the T_d coordination, and the $10Dq$ value is now negative. Cubic symmetry leads to splitting similar to T_d, but the energy difference has a larger magnitude. As compared to the $10Dq$ value for O_h coordination, T_d coordination has a $10Dq$ value of approximately 4/9 of that for octahedral symmetry while cubic has a value approximately 8/9 the value of O_h [40].

3.6.3 Ligand Field (Cluster) and SIAM Models

Building upon the previous two models, the ligand field (or cluster) model includes the electrostatic effects of nearby "clusters" – the ligands and hybridized bonds. By including the central transition metal atom and the nearest ligand atoms in addition to the crystal field and atomic interactions, we have a model which simulates ionic and charge transfer sites whose number varies strongly with the number of $3d$ electrons in the atom of interest.

Finally, a culmination of the previous models, the impurity model – also known as the Single Impurity Anderson Model (SIAM) – includes a band of charge transfer configurations instead of the single charge transfer level seen in the cluster model. This model is necessary to study the multiple charge transfer excitations in RIXS [41–45].

Chapter 4

Molybdenum Disulphide and Cobalt

> The way Moore's Law occurs in computing is really unprecedented in other walks of life. If the Boeing 747 obeyed Moore's Law, it would travel a million miles an hour, it would be shrunken down in size, and a trip to New York would cost about five dollars. Those enormous changes just aren't part of our everyday experience.
>
> – NATHAN MYHRVOLD

As we discussed earlier, the concept of detecting and manipulating electron spin in electronics would advance the current technology well beyond its current capacity. However, very few materials exist that have these electron spin characteristics as well as semiconducting properties. In this chapter, we explore a specific doped semiconductor that falls under the category of dilute magnetic semiconductors, a class of materials that may provide both spin and semiconducting benefits.

Sample	Composition (Co:UDD:MoS_2)	Co Percentage by Mass (wt%)
A	0.095 : 0 : 0.905	10
B	0.182 : 0 : 0.818	18
C	1 : 0 : 3	25
D	1 : 3 : 3	14

Table 4.1: MoS_2 sample composition details. Each sample is shown with its respective composition by mass and percent cobalt by mass.

4.1 Sample Description

We begin with a brief discussion of the material synthesis process before addressing the experimental results. In addition to the four samples mentioned in Section 1.1.1, a fifth sample, MoS_2:UDD (ultra dispersed diamond), was prepared as a model experiment for magnetization testing and will be discussed further below. Table 4.1 shows the four main samples and their compositions. Samples A through C only include cobalt and MoS_2 with cobalt concentrations ranging from $\approx$ 10 wt% to 25 wt%, whereas Sample D includes UDD as well. Each sample was machined in a vibrating mill with a steel mortar using steel balls to induce mixing. The process spanned 8 hours during which the vibration was held constant at a frequency of 16 GHz and amplitude of 2 mm. It was this purely physical process that encouraged the addition of UDD as a means of diminishing the cobalt particle size. Finally, the prepared powders were compressed using approximately 4–6 kN, producing firm pellets.

Preliminary magnetization tests were performed by our collaborator, Dr. Uimin, using a vibrating sample magnetometer operating at room temperature with magnetic fields up to

2.2 MA/m. Samples C and D were each tested, both having the same amount of Co present but Sample D contained UDD whereas Sample C did not. A model sample, UDD:MoS_2, with the same amount of UDD present as Sample D was prepared and tested to aid in identifying iron impurities introduced while milling UDD. The saturation magnetization was measured and compared to the saturation magnetization for the individual components (161 emu/g and 217 emu/g for Co and Fe, respectively).

For the control sample, any magnetization measured is due to iron impurities because there is no cobalt present. A magnetization of 7 emu/g was measured, resulting in the presence of 3 wt% iron ($\frac{7\,\text{emu/g}}{216\,\text{emu/g}} = 0.03$). On the other hand, Sample D showed a magnetization of 23 emu/g, which includes the contribution from the iron impurities seen in the control sample. After subtracting the magnetization due to the impurities (23 emu/g − 7 emu/g = 16 emu/g), the value was then compared to the known value for cobalt, giving 10 wt% of cobalt atoms in a magnetic state ($\frac{16\,\text{emu/g}}{161\,\text{emu/g}} = 0.1$). However, Sample D has a composition of 1:3:3 which should have 14 % cobalt by mass, evidence that 4 wt% of the cobalt have changed state and become non-metallic. These non-magnetic cobalt atoms are attributed to non-magnetic formations such as CoS_2 Finally, Sample C showed approximately 40 emu/g, which is the expected value and shows that the iron impurity is insignificant when UDD is not present. Here $\frac{40\,\text{emu/g}}{161\,\text{emu/g}} = 0.25$, which is equal to the composition ratio of 1/4 = 25 wt% (for 1:3).

4.2 Sulphur $L_{2,3}$ Edge

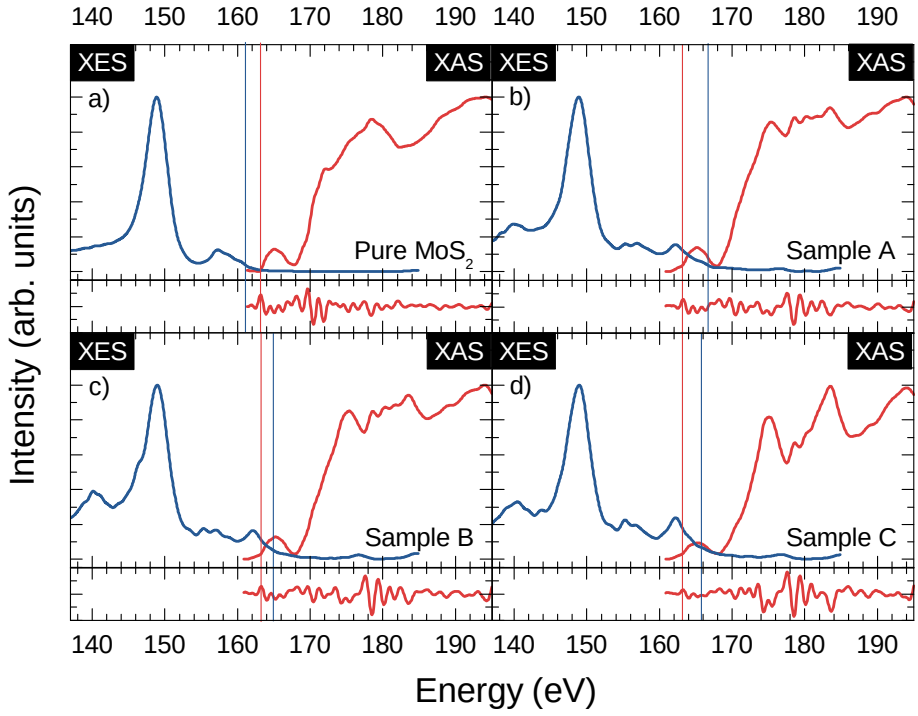

Figure 4.1: Experimental band gaps at the S $L_{2,3}$ edge of Co:MoS_2 with different dopant amounts. Panel a) shows pure MoS_2, panel b) shows Sample A, panel c) shows Sample B, and panel d) shows Sample C. XAS (red) and XES (blue) spectra are shown with XAS second derivatives. The blue and red vertical lines show the valence band maximum (VBM) and the conduction band minimum (CBM), respectively. The CBM is determined using the second derivative method while the VBM is determined by the intersection of two slopes – the background slope and the onset slope. The band gap appears only in pure MoS_2 where the VBM is below the CBM, while the remaining samples are metallic with overlapping valence and conduction bands.

Determining the band gap of a material at the sulphur edge with any amount of certainty is a monumental task. Sulphur edge measurements are wrought with inherently low count rates making it hard to distinguish features, require additional modelling for any estimation of the core hole effect, and experience spin-orbit splitting at the $L_{2,3}$ edge that can lead to yet more uncertainties. Given the difficulty associated with accurately determining the

Band Gap (eV)	Reference
1.29	Gmelin [46]
1.23	Kam *et. al.* [47]
1.06	Ramakrishna Matte *et. al.* [48]

Table 4.2: Literature values for MoS_2 band gap. Various values reported in literature for the band gap of MoS_2. These values include band gaps found variety of experimental techniques as well as calculated band gaps.

band gap at the S edge, mere estimations and overall trends are provided here. Experiments results at the sulphur $L_{2,3}$ edge are shown in Figure 4.1. The valence band maximum and conduction band minimum are determined using the linear approximation method and the second derivative method, respectively, where the chosen method depends on the spectral shape. The sharp onset of the CB allows for the second derivative method to be used, whereas the extremely shallow slope at the upper edge of the VB dictates the use of the linear approximation method. It is important to note that the experiment shows the MoS_2 reference sample to have a band gap of 1.2 ± 0.2 eV, a value that has reasonable agreement with the reported band gaps for MoS_2 shown in Table 4.2.

In Figure 4.1, all variations of MoS_2 have identical conduction band onsets whereas the valence band maximums increase with the inclusion of cobalt (Samples A $\rightarrow$ C) with respect to pure MoS_2. The spreading of the valence band to higher energies can be attributed to the introduction of occupied Co $3d$ states near the valence band maximum. Cobalt states at this energy suggests hybridization between cobalt and sulphur, an indication of Co substitution into the lattice. Additionally, each of the samples containing cobalt has overlapping conduc-

tion and valence bands, showing that cobalt impurities causes the semiconducting MoS_2 to become metallic. Three possible phenomena may be responsible for the metallic nature: (1) excess cobalt in the system forms metallic cobalt clusters; (2) excess Co draws S from the MoS_2 lattice, forming the half- metallic CoS_2 [49, 50]; (3) heavy electronic doping from the replacement of Mo^{4+} with Co^{2+} causes the system to become metallic. Investigation of the Co $L_{2,3}$ data will provide additional insight on this matter.

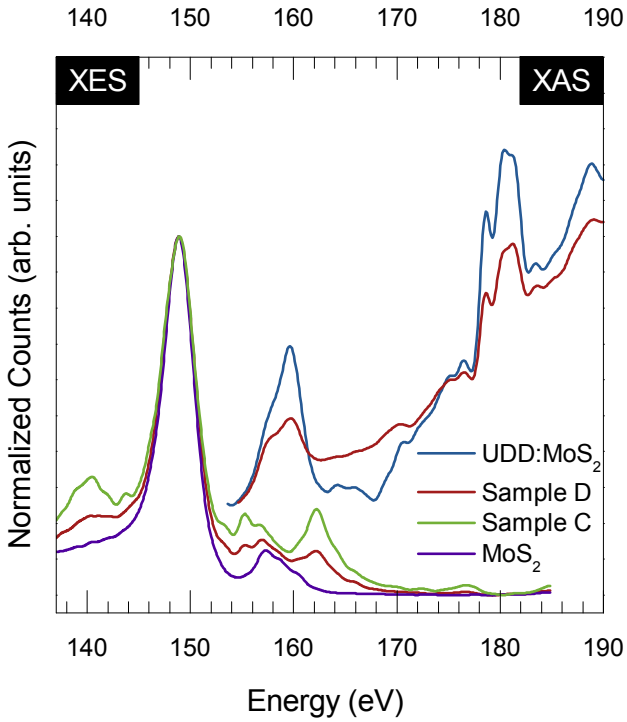

Figure 4.2: Sulphur $L_{2,3}$ data for samples containing UDD. The UDD:MoS_2 and Sample D XAS spectra are shown in blue and red, respectively, along with XES spectra for pure MoS_2, Sample C, and Sample D (green, purple, and red). Both samples containing UDD show XAS spectra significantly dominated by the UDD character. In the XES, pure MoS_2 is given to represent UDD:MoS_2 since UDD seems to have no affect on the valence band (Samples C and D have nearly identical features despite Sample D containing UDD).

Having found that including cobalt makes MoS_2 metallic, this material cannot be used in spintronics applications as discussed in Section 1.1.1. Although it is possible that concentrations lower than 10 wt% may have the intended effect, we conclude that Co:MoS_2 is

metallic and cannot provide the semiconducting properties required for spintronics applications. However, it is possible that these materials may find use in other applications that harness electron spin without requiring a band gap. Techniques such as nuclear magnetic resonance spectroscopy, electron spin resonance spectroscopy, and magnetic resonance imaging all employ materials that are metallic and make use of electron spin.

Earlier in this chapter, Sample D was introduced as a variant to the MoS_2:Co samples. Here we briefly discuss the addition of ultra-dispersed diamond and the characteristics it introduces to the sulphur spectrum. In the sulphur XAS seen in Figure 4.2, UDD dominates the spectral shape, leaving little to no evidence of the changes introduced by the addition of Co, which can be seen when comparing Figure 4.2 with Figure 4.1. In comparison with the samples not containing UDD, the sample containing UDD shows the only variation for the conduction band onset. This conduction band minimum is much lower, making the overlap between the conduction band and valence band greater than in the other MoS_2:Co samples. Despite diamond being an insulator, adding UDD may promote cobalt clustering, resulting in samples that tend towards metallic behaviour rather than insulting. Recall that ultra-dispersed diamond was intended to diminish the size of the cobalt clusters, whereas experiments show that it may be working in the opposite manner. Examination of the cobalt edge below gives more insight into the behaviour of the system when UDD is added.

4.3 Cobalt $L_{2,3}$ Edge

Figure 4.3 shows Co $L_{2,3}$ XAS and RIXS spectra for our selection of samples. This includes three Co:MoS_2 samples (A $\rightarrow$ C) with concentrations by mass ranging from 10 wt% to 25

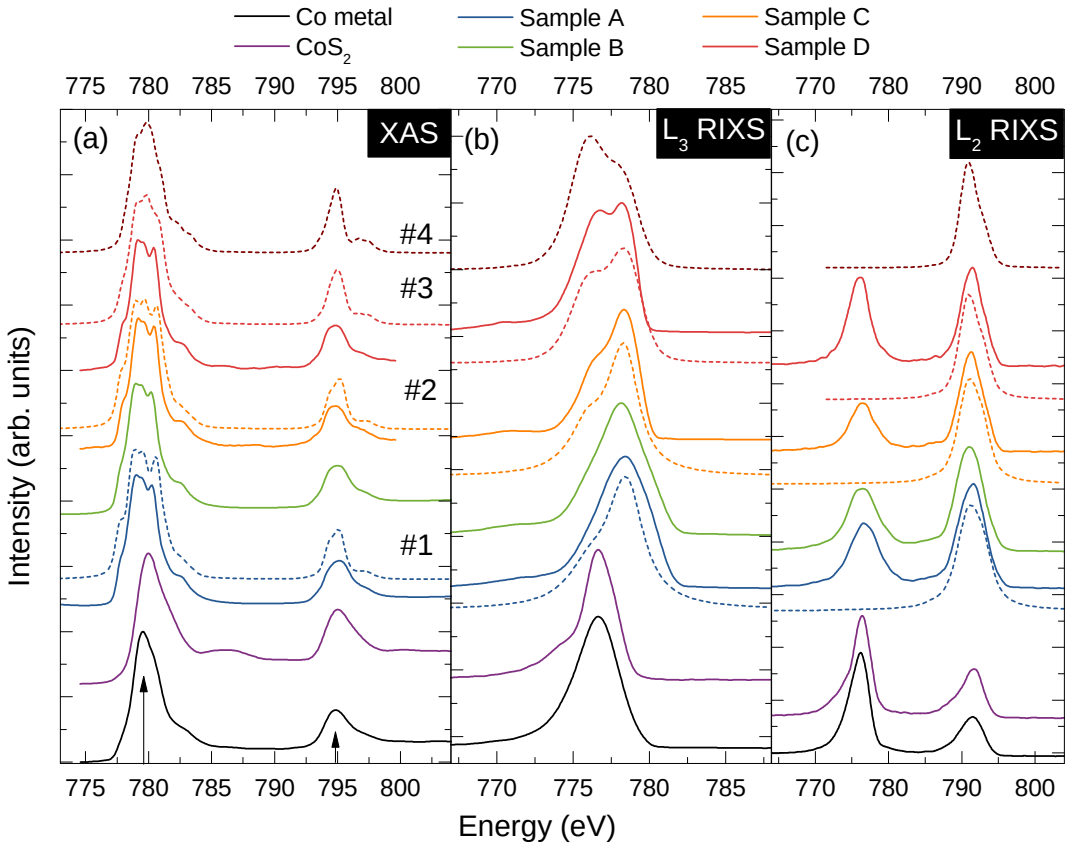

Figure 4.3: Comparison of experimental and calculated Co $L_{2,3}$ spectra. (a) Experimental and calculated $L_{2,3}$ XAS spectra. (b) Experimental and calculated L_3 RIXS spectra. (c) Experimental and calculated L_2 RIXS spectra. L_2 and L_3 calculations arise from setting the excitation energy to the center of each XAS peak, shown by the arrows. Experimental spectra are plotted with solid lines, whereas calculated spectra use dotted lines. Table 4.3 contains the corresponding parameters used for the cobalt calculations (labelled # 1 – # 4).

wt%, and Sample D which contains UDD. Finally, two reference samples, Co metal and CoS_2, are shown. Arrows at 779.6 and 794.8 eV mark the RIXS excitation energies for L_3 and L_2, respectively.

First, we examine the spectral shape of the experimental XAS spectra. Immediately, we see that all variations of Co:MoS_2 have identical XAS, corresponding to the same bonding environments. The similarity between the XAS spectra suggests that the Co might behave similarly in all samples. However, to investigate in more detail the possibility of different

No.	Symmetry	$10Dq$ (eV)	Best Experimental Match
# 1	O_h	0.9	Samples A & B
# 2	O_h	0.85	Sample C
# 3	Mixed O_h & T_d	–	Sample D
# 4	T_d	-0.4	–

Table 4.3: Parameters used for Co XAS and RIXS crystal field model calculations. All calculations are performed using the Co^{2+} ion, a RIXS lifetime broadening of 0.55 eV, and $\kappa = 0.8$ The parameter κ is a rescaling factor used for the intra-atomic Slater integrals, given as fractions of the Hartree-Fock values. Details for calculation # 4 are given in the discussion.

cobalt behaviour in each sample (*i.e.*, substitution, clustering, or forming CoS_2), we can examine the L_3 and L_2 RIXS.

Green, *et. al.* [51] provided excellent evidence for the usefulness of RIXS when XAS fails to provide enough information to determine local bonding. In the current system, RIXS is necessary to determine the details of the Co local bonding environment and how it may change with different cobalt concentrations. L_3 and L_2 RIXS are both included in Figure 4.3; however, we see the majority of differences among the spectra at the L_3 excitation, and so we focus the following discussion on the L_3 panel. In general, higher cobalt concentrations result in the development of a shoulder and eventual peak at 776.5 eV. This lower energy shoulder/peak aligns well with the main peak of the Co metal and CoS_2 spectra.

We can understand the changes in RIXS using our crystal field calculations. Figure 4.3 shows best fit calculations as dotted lines whereas Table 4.3 provides the parameters for each individual calculation. Here we see strong changes in the calculated RIXS after only minimal changes to the $10Dq$ value. It should be noted that these same changes to the $10Dq$ value show very little variation in the calculated XAS spectra. The calculations presented

show good agreement in all cases. Specifically, there is good agreement for all variations of Co:MoS_2 (Samples A $\rightarrow$ C) when $10Dq \approx 0.85$ eV, and agreement between Sample D and calculation # 3 which is a 50:50 summation of $10Dq = 0.85$ and $10Dq = -0.4$. Recall from Section 3.6.2 that a positive $10Dq$ value corresponds to six-fold O_h coordination and a negative value indicates a four-fold T_d environment. We interpret these results below.

First, we consider the cases with low cobalt concentration (Samples A & B). The experimental spectra are well reproduced by calculation # 1 with a $10Dq$ value of 9.0 eV that corresponds to an octahedral bonding environment. One may immediately assume that an octahedral coordination automatically indicates that the cobalt atoms are appearing in the form of CoS_2, which features cobalt atoms in O_h coordination. However, two important features indicate otherwise: (1) the peak at 778.2 eV in the L_3 RIXS does not appear at the same energy as the peak at 776.5 eV for the Co metal and CoS_2 samples, ruling out our initial assumption as a possibility; (2) molybdenum atoms in the MoS_2 lattice sit in the six-fold trigonal prismatic environment, which is a direct variation of the six-fold O_h environment. With these two pieces of information in mind, we are led to believe that the cobalt atoms are substituting directly into molybdenum sites because this accounts for the peak at 778.2 eV while allowing for the O_h coordination. Consequently, the experimental spectra along with the calculated RIXS indicate that at low concentrations, cobalt atoms are substituting directly into the Mo sites.

Next we consider the high Co concentration case (Sample C). Here the best match calculation arises from a $10Dq$ value of 0.85 eV, a value that also corresponds to O_h bonding. However, we now see a shoulder developing at 776.5 eV in the L_3 RIXS. Unlike the lower concentration samples, this shoulder corresponds directly with the peak in the cobalt metal

and CoS_2 L_3 RIXS. Whereas the higher energy peak seen in the low concentration samples is still present, indicating that there is still some substitution into Mo sites, the lower energy shoulder gives evidence for the presence of Co clusters and the formation of CoS_2. Hence, with higher amounts of Co, the system tends towards formation of Co clusters and CoS_2.

Finally, we discuss the case including ultra-dispersed diamond. The best-fit calculation for Sample D is a summation of 50% O_h character and 50% T_d character, suggesting that some cobalt atoms will be in O_h coordination and others will be in T_d. Although the sample still has some O_h character similar to Samples A $\rightarrow$ C, there is obvious tetragonal character when we compare the UDD sample to the pure T_d calculation, # 4 in Figure 4.3. We recognize $10Dq = -0.4$ eV as T_d because tetrahedral coordination corresponds to $\approx$ -4/9 of the $10Dq$ value for octahedral bonding. In the case of Sample D, the O_h character likely arises from a combination of Mo substitution, Co clusters and CoS_2 formation. Conversely, the presence of T_d character is somewhat mysterious until we consider the structure of a diamond lattice. The diamond lattice can be described as a zinc blende structure where both constituent atoms are identical. From that perspective, any cobalt atom entering the diamond lattice would, locally, look like the zinc blende structure where one constituent atom is surrounded by nearest neighbours that are all the other element. Recall that the well-known zinc blende structure has a tetrahedral local bonding environment, indicating that for Sample D, where both Co atoms and UDD are present in equal amounts, Co atoms are also substituting into the diamond lattice.

In examining the relative strengths of the L_2 and L_3 peaks in the L_2 RIXS from the rightmost panel in 4.3, yet more information can be extracted. The ratio (L_3/L_2) of the peaks in the sample containing UDD (Sample D) is much greater than the ratios for any of

the samples not containing UDD, indicating that Sample D may have Co clusters and CoS_2 since their spectra also feature higher ratios. Conversely, the lower ratio in Samples A $\rightarrow$ C suggests that no clustering is present.

Having looked at each case individually, we can now discuss the general trend seen in these materials and the overall impact of the results. First, we see that a low concentration of cobalt atoms produces a structure that allows for the cobalt atoms to substitute directly into the molybdenum sites in MoS_2. Conversely, high concentrations of cobalt atoms produces more clusters of Co metal and CoS_2, especially when UDD is included in the system.

Generally, direct substitution is desirable for the intended applications because it promotes the ability to maintain the majority of properties of the host lattice while introducing the novel properties of the dopant. Additionally, direct substitution allows for a semi-uniform structure under the assumption that the dopant intersperses in an entirely random manner. Uniform structures tend to provide the most consistent properties in materials, an important factor when selecting materials for use in electronics.

4.4 Conclusions

As discussed above, we see some general trends in the Co $L_{2,3}$ data with varying cobalt concentrations in the Co:MoS_2 system. At low to mid concentrations ($\approx$ 10 wt% $\rightarrow$ 20 wt%), Co atoms substitute directly into Mo sites in the MoS_2 lattice. Higher concentrations of cobalt result in some of the cobalt atoms continuing to substitute into the molybdenum sites, whereas excess Co appears as CoS_2 and cobalt clusters, particularly when UDD has been included in the system. It can be assumed that intermediate concentrations feature spectra

that could be deconvoluted as direct combinations of the those measured because of the ability to simulate Co:UDD:MoS_2 using a summation of the O_h and T_d environments. Finally, addition of UDD results in cobalt atoms substituting into the diamond lattice, producing a tetrahedral bonding environment, and as such, the character of Co:UDDMoS_2 is a mixture of tetrahedral and octahedral coordination.

In Section 4.2 we discussed the experimental S $L_{2,3}$ XAS and XES in detail, and here we summarize the findings. After close examination of the estimated band gap for this group of materials, we find two general trends. First, with respect to pure MoS_2 the valence band maximum increases with the inclusion of cobalt. Second, even the samples with the lowest concentrations of cobalt ($\approx$ 10 wt%) are metallic, suggesting that electronic doping arises from the substitution of Mo^{4+} with Co^{2+}.

Overall, the combined sulphur and cobalt data provide us with the tools to evaluate the Co:MoS_2 system for its usefulness in the intended applications. Most importantly, since the semiconducting properties are not maintained after the addition of cobalt at 10% by mass, the system cannot be used in spintronic devices as originally intended. However, given the appearance of Co clusters that would still exhibit the magnetic properties needed in other applications, the system may still be applied to other application in computer technology.

Chapter 5

Copper Oxides Prepared at Varying Pressures

> In 20 or 30 years, you'll be able to hold in your hand as much computing knowledge as exists now in the whole city, or even the whole world.
>
> – E. DOUGLAS ENGELBART

Given the relatively small band gap of naturally occurring copper (II) oxide, CuO, the ability to change its band gap with as simple a process as applying pressure during syntheses would have a massive impact on the way we develop semiconductor technology. In this chapter, we examine the band gap and overall changes to the bonding environment of the copper atoms for a number of CuO samples prepared at different pressures.

5.1 Sample Description

Before delving into the specifics of the results, we begin with a more detailed discussion of the samples and the process used for synthesis. Four samples were used in this study along

Sample	Pressure (GPa)	Treatment	α
Reference	–	–	–
# 1	0.7	HAP	–
# 2	7.1	HAP	–
# 3	8.0	HPT	30°
# 4	8.0	HPT	90°

Table 5.1: Summary of CuO samples. The parameter α represents the angle of shift for the high pressure torsion (HPT) treatment. The samples that did not undergo torsion were instead treated with high axial pressure (HAP).

a reference copper oxide (II) sample. The first sample underwent application of 0.7 GPa of high axial pressure (HAP), where HAP refers to a load applied along the primary axis. A second sample was the result of CuO under 7.1 GPa of HAP. The final two samples both had 8.0 GPa of high pressure torsion (HPT) applied, a process where torsion is applied in addition to a load along the primary axis, but each had different α values. The first of these samples had an α value of 30°, and the other had an α value of 90°. We use α simply to refer to the angle of shift. The above sample descriptions have been summarized in Table 5.1.

These samples were prepared using two variations of pressure application during the synthesis process. Whereas HAP indicates the simple application of high pressure along the primary axis of the anvil setup, HPT includes the addition of axial torsion while pressure is being applied along the axis. Refer to Figure 5.1 for a simplified diagram of the Bridgman anvils used in the synthesis process. As seen in the figure, a disk of the material to be strained is placed between the two anvils and a large compressive stress (typically several

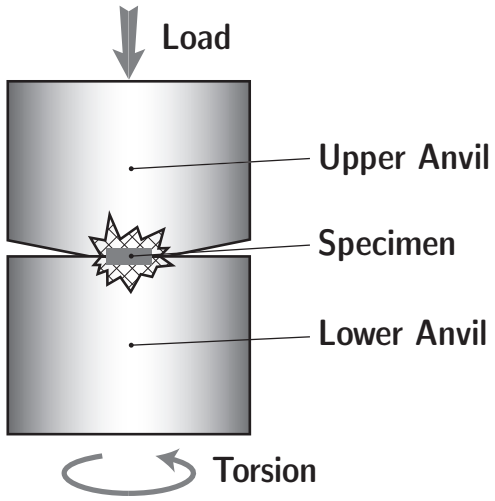

Figure 5.1: Schematic of sample preparation. A disk of material to be treated is placed between two anvils with an axial load applied. Torsion may also be applied through rotation of the lower anvil.

GPa) is applied. For the two samples with only high axial pressure applied, the anvils are merely pressed together at the intended pressure. For those with high pressure torsion applied, one anvil is rotated to create a torsion force. The anvil experienced a rotation of 0.3 rpm (rotations per minute) during the HPT synthesis process. Each of the samples was removed from the anvil after the pressure had been applied, and each showed evidence that the process was inelastic, resulting in permanent changes to the structure.

X-ray diffraction was performed by collaborators on a set of HPT treated samples to examine the effect of the process on the crystal lattice. Figure 5.2 shows the XRD data for two samples that were prepared under 8.0 GPa with $\alpha = 0°$ and $\alpha = 90°$. They are compared to the XRD of a CuO reference sample. In this data, we see that the CuO samples under high pressure have broadened diffraction lines that can be attributed to non-uniform strain, resulting in lattice distortions, a feature important to later discussion.

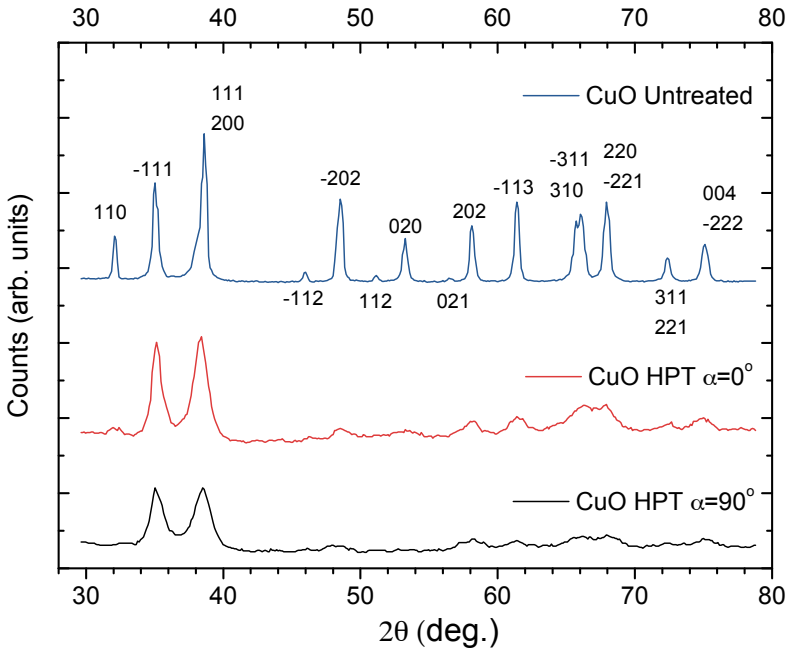

Figure 5.2: Experimental XRD for HPT treated samples. Data is shown for a CuO reference sample and two samples treated with HPT having $\alpha = 0°$ and $\alpha = 90°$.

5.2 Oxygen K Edge

Now that we have discussed the details of the samples and their synthesis, we can take a closer look at the experimental results. Turning our attention to Figure 5.3, we see the experimental band gap as determined by the oxygen K XAS and XES for all four samples and the CuO reference. Each of the samples shows a valence band maximum at the same location, but the conduction band minimum shifts to higher energies as the pressure applied is increased. With this shift to the conduction band, we see the band gap widen with applied pressures greater than or equal to 0.7 GPa. This tendency toward a larger band gap can be attributed to the lattice distortions seen in the XRD (Figure 5.2). It should be noted that the jump from a 2.0 ± 0.2 eV band gap in the reference material to a 2.3 ± 0.2 eV band

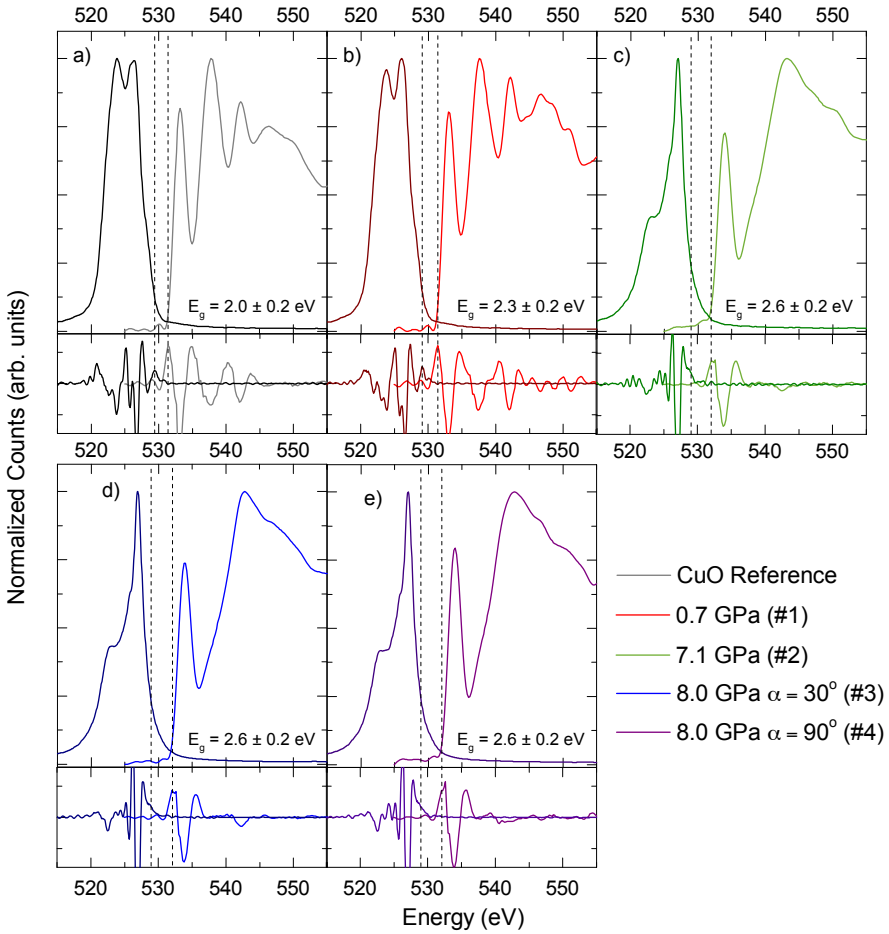

Figure 5.3: Experimental band gaps of CuO prepared at different pressures. From left to right: a) Reference CuO; b) CuO prepared at 0.7 GPa; c) CuO prepared at 7.1 GPa; d) CuO prepared at 8.0 GPa with $\alpha = 30°$; and e) CuO prepared at 8.0 GPa with $\alpha = 90°$. XAS (red) and XES (blue) spectra are shown with their corresponding second derivatives. The left dotted line shows the valence band maximum, whereas the right dotted line shows the conduction band minimum. The band gap is the difference between the two.

gap after application of 0.7 GPa indicates that there may be a threshold pressure below 0.7 GPa at which the band gap increases beyond the 2.0 ± 0.2 eV of the CuO reference sample. Unfortunately, no evidence of a threshold can be seen with this particular sample set.

In the XRD data above, we saw evidence that higher synthesis pressures caused some distortions to the CuO crystal lattice. Those lattice distortions could be a direct cause of the increasing band gap in the oxygen data. Given that these changes are only occurring in the oxygen spectra, it suggests that the lattice distortions are appearing in the form of oxygen

vacancies forming within the lattice. In Section 5.3 we will investigate this claim further by examining the copper spectra.

Early on, we introduced the idea of band gap engineering in relation to this group of materials. Given the increasing band gap with the addition of pressure during the synthesis process, this group of materials remains a strong candidate for band gap engineering. While most band gap engineering requires a rather complicated process, the simple application of high pressure and torsion to a disk of material is one of the least complex methods for engineering a band gap. Having a simplistic approach for engineering larger band gaps would make materials synthesis more efficient and cost-effective.

It is important to note that the experimental band gaps reported here may have overestimated the band gap. The band gap of copper (II) oxide is reported as 1.7 eV [52] – 0.3 eV smaller than the measured CuO reference sample band gap – however, the investigation was performed using photoemission spectrscopy, a method that often overestimates the gap with respect to soft x-ray methods. Consequently, the reported values are estimated to be at least 0.3 eV larger than in reality. Under these assumptions, the band gap still opens with higher preparation pressures, but the system retains a band gap that is tunable in a range still useful in traditional semiconductor applications.

5.3 Copper $L_{2,3}$ Edge

In the previous section, we discussed the oxygen K spectra and the changes in band gap for each of the samples. Here we look at the copper $L_{2,3}$ spectra shown in Figure 5.4 and examine how features at the copper edge are related to the changes we see at the oxygen

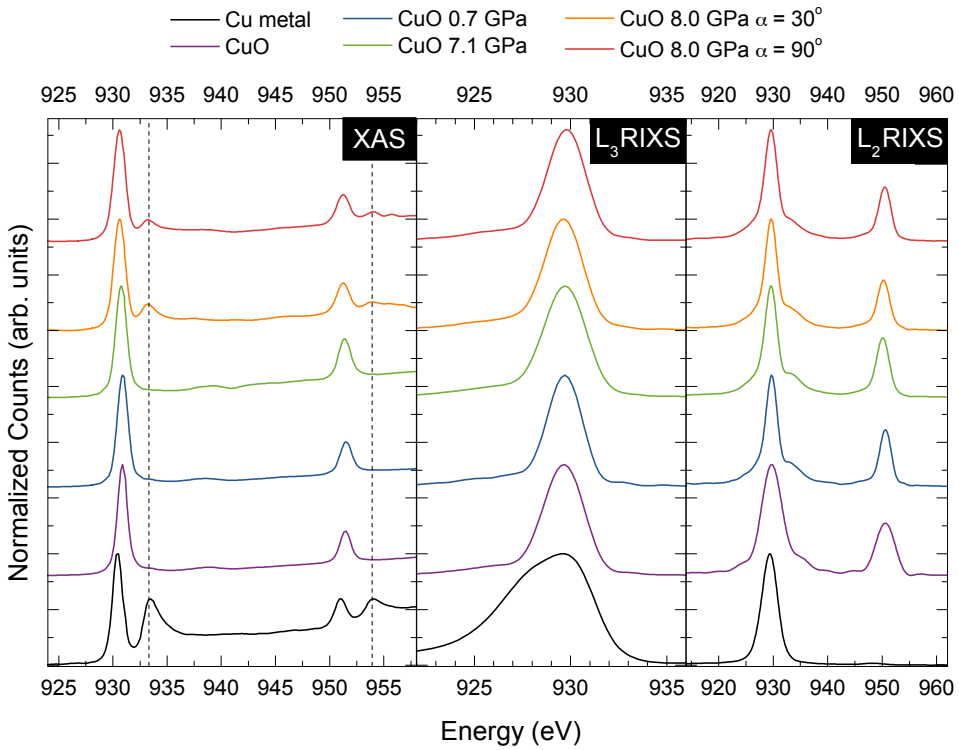

Figure 5.4: Experimental Cu $L_{2,3}$ XAS and RIXS spectra for CuO prepared at various pressures. The leftmost panel shows the experimental XAS, the middle panel shows the L_3 RIXS, and the rightmost panel shows the L_2 RIXS.

edge. Overall, the most noticeable aspect of the copper edge is that all of the samples look incredibly similar. The only changes evident in either the XAS or RIXS are the appearance of small peaks (indicated by the dotted line) following the primary L_2 and L_3 XAS peaks in the samples prepared at 8.0 GPa. The two samples treated with only axial high pressure (0.7 and 7.1 GPa) have spectra nearly identical to the untreated CuO, indicating that there are no changes to the Cu oxidation state. On the other hand, application of high pressure torsion is accompanied by the appearance of the additional features mentioned above that coincided with features in pure Cu metal. Recall the evidence of lattice deformation in the XRD (Figure 5.2) for samples treated with HPT and the indication in the oxygen spectra (Figure 5.3) that

oxygen vacancies began forming after the addition of higher pressures. Similarly, the copper spectra for the HPT treated samples show a variation to the copper valency in the form of Cu^0 and Cu^{1+} species that could arise from such oxygen vacancies. As such, we see strong evidence suggesting that the application of high pressure torsion causes lattice distortions in the form of oxygen vacancies, giving rise to variations in the copper oxidation state.

It is important to note that although the multiplet calculations are normally very useful in determining the oxidation state and bonding environment of transition metal atoms, the XAS of CuO cannot be simulated. In a Cu^{2+} system like CuO, the excited final state used to simulate XAS has a full $3d^{10}$ orbital. The full shell gives no information and will always show only a single peak in each of the L_2 and L_3 regions. On the other hand, RIXS simulations of CuO can give a little more information because it has electrons in the $3d^9$ configuration in the final state, giving rise to multiple combinations of orbitals in which those 9 electrons may arrange themselves. Although one can determine the crystal field by analyzing those RIXS simulations, the experimental RIXS shows no information or variation with increasing pressure, and as such, no RIXS multiplet calculations are presented here.

The lack of distinguishing changes to the copper oxidation state suggests that many properties of the material, with the exception of band gap, may remain relatively constant even beyond 8.0 GPa of pressure. It is only the samples treated with high pressure torsion that show any change to the Cu valency, indicating that there is either a pressure threshold at which the copper oxidation state begins to change, or that the change is solely because of the torsion the lattice experiences. Under the assumption that the Cu electrons remain relatively unaffected, this particular treatment and material choice would be well-suited for applications requiring an engineered band gap.

5.4 Conclusions

Experimental x-ray absorption and emission spectroscopy on the oxygen K edge has shown that the band gap of CuO increases with increasing pressure for high axial pressure and high pressure torsion treatments. Having seen a 0.3 eV increase in band gap for the sample treated with the lowest pressure (0.7 GPa), there still remains the possibility of a lower threshold pressure at which the band gap would start to increase beyond the 2.0 eV of the reference CuO. In the same manner, this group of samples offers no indication of a limit to the trend, but it is reasonable to believe that at even greater pressures the structure would undergo major distortions causing the trend to cease. As such, further investigation would be required to fully characterize the ability to engineer the band gap in pressure-treated CuO.

Examining the complimentary copper $L_{2,3}$ edge, we find little to no changes in the XAS and RIXS with increasing pressure. The unchanged spectra are a good indication that, aside from the changes to the band gap, other material properties remain unaffected with increasing pressure. As with the band gap, there still may be a greater pressure that would cause this tendency to fail, potentially causing extreme changes to the material properties if the structure becomes drastically distorted or unstable.

Overall, we can say with certainty that treating CuO over this range of pressures results in stable materials with a tunable band gap while maintaining all other properties. As such, this group of materials is an excellent candidate for wide band gap semiconductor applications and can be tuned to suit a variety of needs. Pressures above 8.0 GPa and below 0.7 GPa should still be tested using the same methods appearing above to completely describe the system and potentially expand on it's useful pressure range.

Chapter 6
Molecular Systems

The science of today is the technology of tomorrow.

– EDWARD TELLER

In addition to the projects described in the previous chapters, I was also involved in the work for two additional projects that both resulted in manuscripts that were published in peer-reviewed journals. They are discussed separately from the previous discussion because their experimental and theoretical details can already be found in each of the manuscripts.

6.1 Potassium-doped Anthracene and Phenanthrene

The bulk of the work for this project spanned the two years I spent as a summer student under Dr. Moewes, and the work was published soon after I began work as a graduate student. It served as an excellent introduction to x-ray spectroscopy and condensed matter physics, allowing me to explore the concepts in a self-taught and self-motivated environment. Having learned some of the techniques that I would later use in my graduate studies, I felt

as if my work served a much greater purpose.

Although the work did not introduce me to all of the techniques I would later use, it gave me a solid basis for my future work. In addition to having some involvement with the synthesis process, I was heavily involved the XAS experiments and calculations that simulated XAS for molecular systems using a program called SotBe. StoBe is a robust program that can simulate XAS and other x-ray excitation experiments for systems with a set molecular pattern. It excels when the system can be described by a single molecule as opposed to a repeating lattice because it simulates a direct excitation of each atom given as input, allowing for an overall excited state to be determined from the sum of the excited states of each atom. Further details for the experimental and theoretical background can be found in the manuscript, which is reproduced below.

The manuscript was published in the Journal of Physical Chemistry C in August 2013. It can be found using the reference: Pitman, A. L., Mcleod, J. A., Khozeimeh Sarbisheh, E., Kurmaev, E., Müller, J., Moewes, A. X-ray Spectroscopic Study of the Conduction Band of K_3:Anthracene and K_3:Phenanthrene. *J. Phys. Chem. C.* **117**, 19616. I am listed as first author because I was not only responsible for drafting the manuscript but also performed the tasks described above. The manuscript is reproduced in full below.

X-ray Spectroscopic Study of the Conduction Band of K_3:Anthracene and K_3:Phenanthrene

Amy L. Pitman,[*,†] John A. Mcleod,[†] Eleheh Khozeimeh Sarbisheh,[‡] Ernst Kurmaev,[§] Jens Müller,[‡] and Alexander Moewes[†]

[†]Department of Physics and Engineering Physics and [‡]Department of Chemistry, University of Saskatchewan, Saskatoon, SK, Canada

[§]Institute of Metal Physics, Russian Academy of Sciences, Yekaterinberg, Russia

Keywords: XAS, DFT, superconductivity, band structure, DOS

Abstract

We study anthracene and phenanthrene doped with potassium using x-ray absorption spectroscopy and electronic structure calculations. In addition, a comparison of molecular orbital calculations and solid state density functional theory calculations are presented. We find that potassium-doping partially populates the LUMO level of anthrancene and phenanthrene, and that both the measured and calculated electronic structures of the doped systems are quite different from that of the pristine molecular systems. This suggests that the extra charge carriers in the doped-system are responsible for the increased conductivity and greater intermolecular interaction. Finally, our calculations suggest that both K_3:phenanthrene and K_3:anthracene have a reduced or non-existent band gaps as compared to their pure counterparts, further supporting the conclusion that doping is responsible for increased conductivity.

Introduction

Organic molecular solids have recently come into the spotlight for several important applications. One of the main areas of research is organic electronics [54, 55], more specifically organic light emitting diodes, organic thin film transistors, and organic field effect transistors. Furthermore, research into organic electroluminescence materials [56, 57] and organic photovoltaics [58, 59] has also received a great deal of attention. Another major area of interest in these organic molecules is superconductivity, opening the door to advances in digital circuitry, magnetic resonance imaging, and improved power transmission among others [60–62]. However, the mechanism driving superconductivity in organic materials remains unknown, motivating a multitude of further studies including this work.

A number of studies have reported superconductivity at temperatures ranging from 6.5 – 33 K [63–70] in π–electron network materials when excess charge is introduced via doping. Thus, organic superconductors are highly associated with the π–electron networks that appear in a number of hydrocarbons. More recently, Mitsuhashi *et al.* reported superconductivity at temperatures up to 18 K in potassium-doped picene [71]. It was suggested that within the lowest unoccupied molecular orbital (LUMO), the density of states (DOS) of the LUMO+1 band might be responsible for the superconducting transition. Following this discovery, several groups conducted studies attempting to explain the mechanism of superconductivity in K_3:picene [72–74] including examining its electronic structure [75].

Inevitably, these discoveries led to a number of studies of the electronic structures of these aromatic compounds and how they are affected by dopant concentrations. Roth *et al.* reported a shift of LUMO orbitals to lower energies when potassium dopants were introduced

to K:coronene [63] and K:picene [75]. Furthermore, in examining K:picene through electron energy loss spectroscopy (EELS), an effect similar to the attenuation of x-rays measured in x-ray absorption spectroscopy, Roth *et al.* presented an evolution showing loss function intensities shifting to lower energies as potassium concentration increased [75].

Further motivation for this work presented itself when Wang *et al.* [76] published their findings of superconductivity at 5 K for K_3:phenanthrene. In this work, we examine pure and potassium doped anthracene and phenanthrene with x-ray absorption spectroscopy (XAS) and theoretical methods to determine the influence of potassium on the LUMO structure of these materials.

Experiment and Calculations

Synthesis of K_3:Phenanthrene and K_3:Anthracene

In preparing the doped samples, synthesis was performed in a manner similar to those described by Mitsuhashi *et al.* [71] and Wang *et al.* [76]. To begin all starting compounds were purchased from Alfa Aesar (99% purity or higher). Phenanthrene (1.52 g, 8.53 mmol) and potassium (1.04 g, 26.6 mmol) were combined in a Schlenk flask under N_2 atmosphere in a glove box (MBraun). The mixture was heated under nitrogen at 200 °C using a sand bath and after 24 h the sand bath was removed. Then the reaction mixture was left unheated for another 24 h. Using the same method, K_3:anthracene was synthesized from anthracene (1.52 g, 8.53 mmol) and K (1.03 g, 26.3 mmol). The prepared samples attained a black hue, noticeably different from the white color of the pure powders of the initial organic compounds. Such a change in color was also reported for doped phenanthrene by Wang *et al.* [76] and for doped picene by Mitsuhashi *et al.* [71]. To examine the influence of oxidation, some of

the doped samples were exposed to air resulting in a change of color from black to white. A similar behaviour as reported by Wang *et al.* [76] for doped phenanthrene.

X-Ray Absorption Spectroscopy Background and Procedure

Before discussing the procedures taken to measure the x-ray absorption spectroscopy spectra for each of our samples, it is important to briefly discuss the technique. X-ray photoabsorption results in the ejection of a photoelectron creating a core hole. The core hole is filled by an electron in one of two processes where each can be measured by beamline instruments. Being a direct result of the core hole created by absorption, it is therefore a measure of the absorption cross section. The absorption edge in XAS is a result of the excitation of a core electron to a continuum of final states (the conduction band). These transitions only occur if the energy of the incoming photons exactly matches the energy difference between the initial state and an unoccupied state. Thus, a scan over photon energies results in an XAS spectrum showing the dependence of the absorption cross section on photon energy. For a more detailed discussion see the review by Hähner [77]. It must also be noted that unfilled core holes may cause a significant shift in the electronic structure due to the rearrangement necessary to minimize the energy of the ground state. This effect is primarily of concern in the theoretical calculations discussed in the next section.

Now that we have established an idea of what XAS probes, we present the outline of the procedure used to take these measurements. XAS measurements were performed at the Canadian Light Source (CLS) Spherical Grating Monochromator (SGM) beamline [78]. We pressed the prepared powders into pure sodium metal in a nitrogen atmosphere and then reduced the pressure to 10^{-7} torr. We used pure sodium because its amount of metallic lustre

provided a qualitative probe of the presence of oxygen. The room-temperature XAS measurements were performed in the surface-sensitive total electron yield (TEY) mode, in which the sample is connected to ground through an ammeter and the measured current is proportional to the density of states in the sample. TEY was chosen to easily detect surface oxidation, allowing for a qualitative measure of oxygen presence in addition to the pure sodium mentioned above. In addition to the samples mentioned above, we also measured two anthraquinone powders (1,4– and 9,10–; Alfa Aesar, 99% purity) and 9,10–phenanthrenequinone powder (Alfa Aesar, 95% purity) for comparing features related to oxygen content. The energy calibration for each system was based on the calibration required for the C 1s XAS spectrum of planar graphite, where the graphite π^* feature was shifted to 285.4 eV.

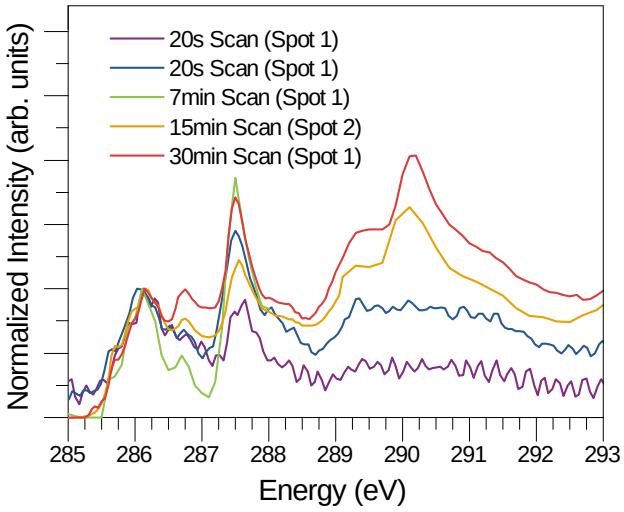

Figure 6.1: Effect of radiation damage on the near-edge fine structure. Spectra are labelled in order of increasing radiation exposure (top to bottom in legend).

To minimize damage done to the samples during measurement, we repeatedly measured each sample in new positions using the Fast Scan capabilities of the SGM beamline. These 20 second scans, which minimized the radiation exposure of the sample, compared against

longer measurement times showed that the region of interest closest to the C $1s$ transition edge remained unaffected (Figure 6.1). While the region from 285.5 eV to 286.5 eV retained similar fine structure throughout all measurements, Figure 6.1 shows two peaks increasing in intensity with radiation exposure, most predominantly the feature at 287.5 eV. Since our region of interest was shown to remain unaffected by radiation damage, we chose the 15 min scan to represent anthracene for the remainder of the discussion due to its high resolution near-edge fine structure.

First Principles Calculations

We performed theoretical calculations using StoBe, a program that takes its starting point from free molecules, and WIEN2k, which assumes a periodic structure. Previously we considered the creation of a core hole during the x-ray transition. It is important to note that while StoBe creates a structure using a core hole perturbed conduction band, WIEN2k only employs the ground state conduction band in determining electronic structure. Below, we will provide additional details on the operation of these both StoBe and WIEN2k and elaborate on the calculations performed for our particular systems.

StoBe is a density functional theory (DFT) code that uses a linear combination of atomic orbitals basis to calculate the electronic structure and x-ray spectra (including calculation of the x-ray transition) of isolated molecules [79], and is therefore ideal for studying molecules such as phenanthrene and anthracene. We used both orbital and auxiliary basis sets corresponding to each atom in the molecule (`O-CARBON (7111/411/1), A-CARBON (5,2;5,2), O-HYDROGEN (41/1*), A-HYDROGEN (3,1;3,1)`) and an exchange-correlation functional formed by the two GGA exchange functionals, BE88 [80] and PD86 [81]. To ex-

plicitly model the x-ray transition, the simulation is repeated for each carbon atom present, modifying the orbital basis sets to allow for only a single excited atom in each iteration. An additional model core potential basis set was then used for the excited carbon atom in the system and non-excited atoms were given modified orbital and auxiliary basis sets to allow for individual atoms to be excited.

WIEN2k is a DFT code that uses a linearized augmented plane wave basis to calculate the electronic structure of periodic crystals [82], and is therefore suitable for studying crystalline doped (and undoped) phenanthrene and anthracene. For the WIEN2k calculations of pure phenanthrene and anthracene, we started with reported crystal structures [83, 84]. A first-principles density functional theory study of K_3:phenanthrene [85] provided its initial WIEN2k structure, while for K_3:anthracene we started by adding 6 K atoms to the unit cell of crystalline anthracene. In all cases the atomic positions were optimized to minimize interatomic forces. We used atomic sphere radii of 1.2, 0.65, and 1.8 Bohr for C, H, and K, respectively, and the product of the smallest sphere radii and the largest plane wave wavenumber ($RMT_{min}K_{max}$) to 4.0. For optimizing the crystal structure, we used a special k-point grid of 12 points (the grid was $2 \times 2 \times 3$, or a permutation thereof, as appropriate for crystal structure) and increased the grid to 60 points (the grid was $3 \times 4 \times 5$, again as appropriate for the crystal structure, although the grid for phenanthrene was actually 72 points split as $3 \times 4 \times 6$) for calculating the electronic structure.

As mentioned above, with StoBe, we were able to calculate the C K XAS spectra for phenanthrene and anthracene in a manner that included the effect of the core hole and the x-ray transition on the electronic structure. With WIEN2k, we calculated the C K XAS spectra for all compounds using the ground state conduction band and the appropriate transition

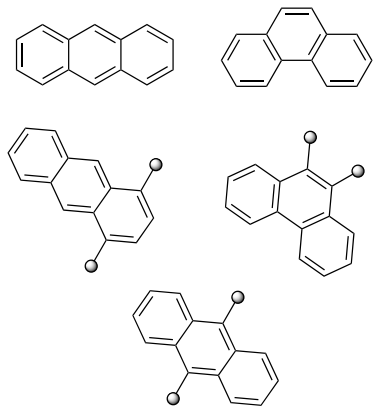

Figure 6.2: Molecular structure of pure samples used. *Top Left*: anthracene; *Top Right*: phenanthrene; *Middle Left*: 9,10-anthraquinone; *Middle Right*: 9,10-phenanthrenequinone; *Bottom*: 1,4-anthraquinone.

matrix elements [86]. We did not attempt to calculate the influence of the core hole due to the negligible effect it had on a preliminary phenanthrene calculation as compared to StoBe. It must also be noted that StoBe is unsuitable for periodic structures and cannot properly incorporate interstitial doping into it's molecular model, therefore, it was unable to predict spectra of the highly crystal-dependent doped samples.

Results and Discussion

Phenanthrene and anthracene are organic molecules that are formed of fuzed benzene rings (Fig. 6.2). As such, the XAS spectrum of benzene proves to be an important part of the XAS spectra of these individual molecules. It has been reported that the XAS spectra of molecules comprised of `n` benzene rings is similar to `n` shifted copies of benzene's XAS spectrum [87]. However, when dopant atoms are introduced to these systems, the fine structure associated with benzene and similar organic molecules is lost [72]. As such, XAS is a useful probe of subtle changes in the electronic structure for these alkali-doped systems.

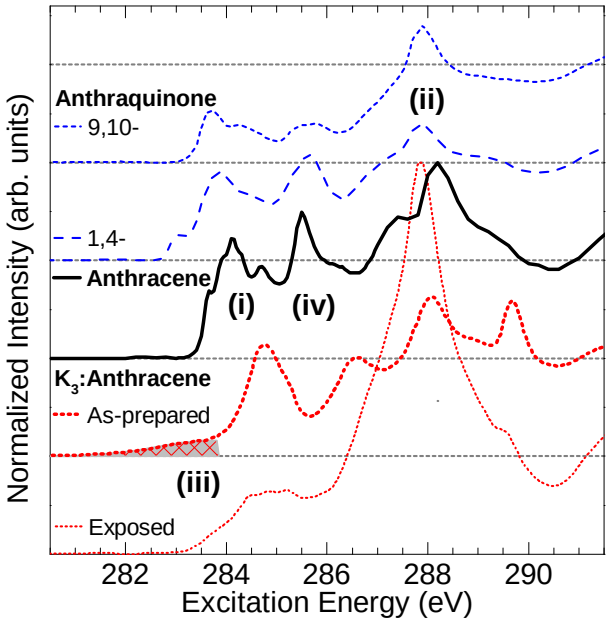

Figure 6.3: C 1*s* absorption spectra of anthracene-based samples. *From top to bottom*: 9,10-anthraquinone, 1,4-anthraquinone, anthracene, K_3:anthracene, K_3:anthracene after exposure to air. Four features are noted: (i) fine structure of molecular solid; (ii) beam damage region relating to oxygen content; (iii) LUMO produced with K-doping; (iv) feature associated with beam damage unrelated to oxygen.

Experimental XAS

Figure 6.3 shows the measured XAS spectra of anthracene, the two anthraquinones, K_3:anthracene, and K_3:anthracene after being exposed to air. All of these spectra, as well as those shown in Figure 6.4 were normalized with the beam current measured by a gold mesh on the CLS SGM beamline. Three key features are identified in these spectra, along with a fourth of less significance. The first is the fine structure in the π^* resonance of pure anthracene (see feature (i) in Figure 6.3), the second a shift in the peak attributed to beam damage induced by the presence of oxygen, and the third the low-energy pre-edge produced by doping.

The fine structure in feature (i) that appears on the scale of 0.1 eV, as previously reported [87], can be attributed to the interaction and localization of the π-electrons in the

hybridized sp^2 orbitals. This low energy fine structure around 284 eV is reduced and smeared out as the sample is repeatedly measured, while the peak at 288 eV grows in intensity (see feature (ii) in Figure 6.3). Both of these phenomena suggest that all of these organic materials are sensitive to beam damage. However by performing short, rapid measurements of small portions of the total spectrum at fresh locations on the samples we were able to measure the XAS spectra with minimal beam damage.

The second key feature is related to both beam damage, as mentioned above, and oxidation (see feature (ii) in Figure 6.3). Beam damage typically refers to the chemical bonding changes due to interaction with the incident radiation. This includes the breaking and rearranging of bonds and typically reveals itself as a growing spectral feature. In many cases radiation causes the valence structure to change promoting a specific excitation and resulting in a strong feature. We identify this particular beam damage as a result of the presence of oxygen. While the feature grows with increasing beam damage, it is important to note that at feature (ii) there is a small difference in the peak energy between the systems that do contain oxygen (both anthraquinone samples and the exposed K_3:anthracene) and the systems that should not (anthracene and K_3:anthracene). This suggests that our K_3:anthracene sample was minimally oxidized. The intensity of this "damage" peak in exposed K_3:anthracene suggests that the energy released by the oxidation of the K–atoms was sufficient to break apart some of the anthracene molecules.

Finally, the third key feature is found in the broad pre–edge to K_3:anthracene (see feature (iii) in Figure 6.3), indicating the low energy conduction band that is produced by K–doping. Through EELS, Roth *et al.* [75] also present a similar trend. This feature suggests that K–doping gives rise to improved conductivity.

It must also be noted that pure anthracene as well as its anthraquinone counterparts all exhibit a peak around 285.5 eV in Figure 6.3, denoted by (iv). This feature is attributed to radiation damage unrelated to the oxygen content of the sample, but rather the breaking of bonds in the σ^* region and other general changes to the electronic structure due to interaction with x-rays.

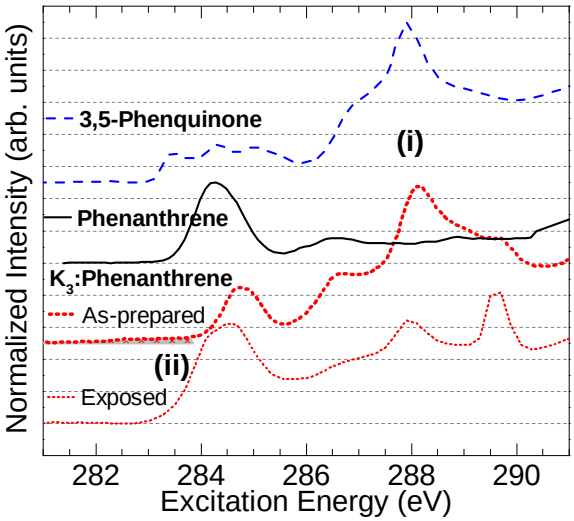

Figure 6.4: C 1*s* XAS spectra of phenanthrene-based samples. *From top to bottom*: 9,10-phenanthrenequinone, phenanthrene [88], K_3:phenanthrene, K_3:phenanthrene after exposure to air. Two features are noted: (i) beam damage region related to oxygen; (ii) LUMO produced by K doping.

Examination of the phenanthrene counter-part shown in Figure 6.4 reveals similar features such as the beam damage peak due to the presence of oxygen and the pre-edge conduction states. It must be noted that pure phenanthrene is not vacuum compatible, and, therefore, its XAS spectrum could not be obtained. However, an absorption spectrum taken under helium atmosphere is included [88], showing strong agreement with the calculated spectra discussed below. As expected the addition of the K–dopant introduces enough change to the electronic structure of phenanthrene to allow K_3:phenanthrene to be ultra-high vacuum

compatible.

Feature (i) in Figure 6.4 shows the same beam damage peak as was evident in the anthracene measurements. A similar behaviour is observed, including the energy location of the peak at 288 eV. This further supports that this peak is caused by beam damage and is related to the oxygen content of the sample. Also similar to the anthracene measurements, feature (ii) shows pre-edge conduction states appearing in K_3:phenanthrene. This feature is considerably weaker than in K_3:anthracene, but still suggests an increase in the sample's room temperature conductivity. Whether this is connected to the low temperature superconductivity reported by Wang *et al.* [76] requires further studies.

In both Figure 6.3 and Figure 6.4, the XAS spectra of K_3:anthracene and K_3:phenanthrene look nothing like their pure counterparts despite the simplicity of intercalation as the intercalation in these systems appears as dopant atom lying in the spaces between molecules. The interaction with the potassium dopant atoms likely destroys the fine structure associated with the isolated molecules, resulting in a drastic change to the electronic structure and giving an XAS spectrum similar to that of a bulk crystal.

Calculated Electronic Structure

It is also important to examine the density of states for the studied systems to further understand the changes seen between the doped and undoped systems. Despite the significant changes to the electronic structure when potassium is added to both the anthracene and phenanthrene systems, the same K-doping does not significantly change the basic structure of the calculated DOS (Figure 6.5). The only clear change is that some lower energy orbitals of the LUMO become part of the highest occupied molecular orbitals (HOMOs) in both

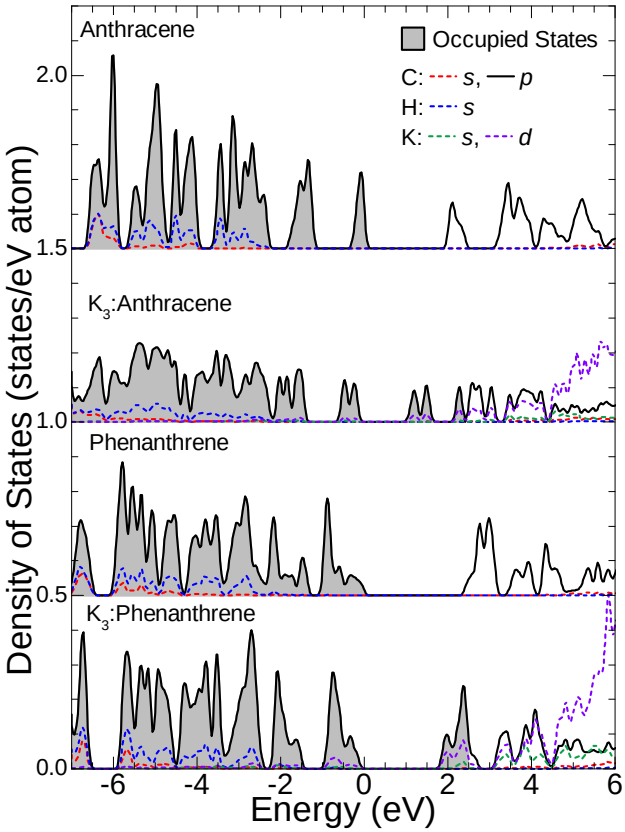

Figure 6.5: DOS calculations performed by WIEN2k for anthracene, K_3:anthracene, phenanthrene, K_3:phenanthrene. Of particular importance is the transfer of LUMO states to HOMO states with introduction of K. Here 0 eV corresponds to the top of the HOMO in undoped phenanthrene and anthracene.

systems. In both of the doped systems, the Fermi level remains unshifted to better show the transition of states from LUMO to HOMO. This tendency for K-doping to move molecular orbitals to lower energies was also suggested by Roth *et al.* [75].

The HOMO-LUMO gap of anthracene and phenanthrene is calculated to be 2.012 eV and 2.418 eV, respectively. In the literature, the gap of anthracene is still disputed, but is generally agreed to be between 1.84 eV and 4.4 eV [89–91], and our calculated value falls within this range. Phenanthrene has a reported HOMO-LUMO gap of approximately 3.5 eV [92]. In contrast K_3:anthracene was calculated to have a very small gap of 0.101 eV, suggesting that

potassium doping has a smaller effect on improving the conductivity of anthracene than K_3:phenanthrene, whose calculations show it to become metallic with doping.

As expected, the HOMO/LUMO states are primarily of C $2p$ character, and in the K_3:anthracene and K_3:phenanthrene unoccupied states, a significant amount of K $3d$ character is found.

Calculated XAS

In addition to discussing the XAS of the different systems measured, we also present calculations from WIEN2k and StoBe to evaluate the performance of each model and further understand their relation to the experimental measurements. Comparing the calculated XAS spectra to those measured experimentally (Figure 6.6) shows that the calculations of both pure substances fail to reproduce the fine structure at lower energies, but otherwise show reasonable agreement with the measured spectra.

The anthracene-based spectra show the WIEN2k and StoBe calculations to be very similar and the WIEN2k method features LUMO states below the main π^* peak as expected. The close similarity between the two spectra despite WIEN2k excluding the core hole effect where StoBe includes it suggests that the core hole present in the XAS transition does not cause any significant distortion to the shape of the unoccupied molecular orbitals (UMOs). If we assume that the core hole only shifts the UMOs to lower energies, we can shift the WIEN2k calculation by 0.7 eV with no adverse effect. Following this shift, we see reasonable agreement between the calculation and experiment for some of the features of K_3:anthracene. It may be possible that the doping is inhomogeneous, resulting in underdoped areas that result in weaker characteristic features. Thus it is reasonable that the near edge states identified by

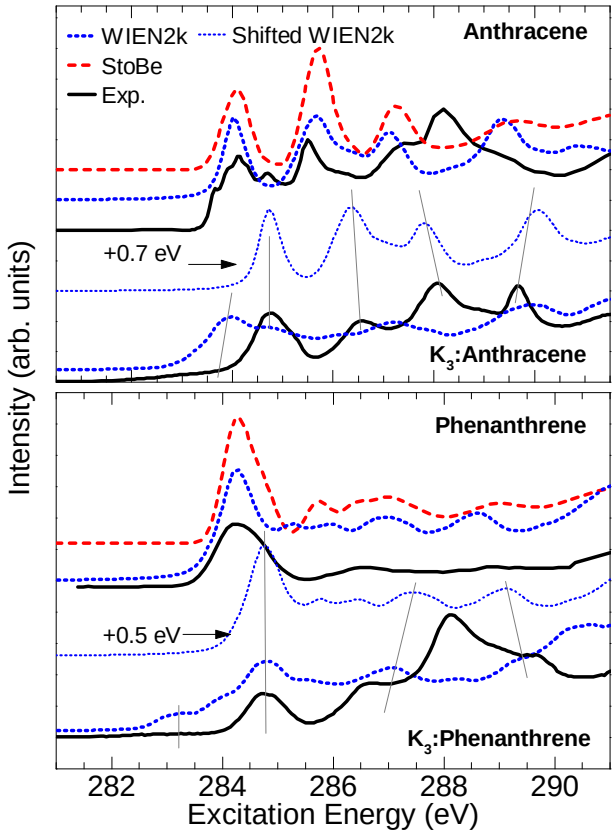

Figure 6.6: XAS measurements and calculations performed by WIEN2k and StoBe for anthracene, K_3:anthracene, phenanthrene, and K_3:phenanthrene. Shifting of pure anthracene and phenanthrene WIEN2k spectra results in reasonable agreement between some features in the doped samples. The energy shifts to align the π^* resonances in the calculated spectra of undoped anthrancene and phenanthrene with the π^* resonances in the calculated spectra of K_3:anthracene and K_3:phenanthrene are noted in the figure. The experimental measurement for phenanthrene is provided by Gordon *et al.* [88].

features (iii) and (ii) in Figures 6.3 and 6.4, respectively, are weaker than our calculation predicts. These differences may also be caused by a strongly over-emphasized dependence on the dopant in the model, therefore underdoping of the samples and over-emphasis in the model may both have an influence on the difference between the calculated and experimental systems.

Similar arguments may be made for the phenanthrene-based spectra also shown in Figure 6.6. We see both measurements to be in good agreement, so we make the assumption that

the core hole merely shifts the energy of the UMOs as before. In contrast, we see that agreement with the K_3:phenanthrene measurement occurs when the WIEN2k calculation is shifted upward by 0.5 eV. Once again, we also see that for K_3:phenanthrene, the calculation and experiment show a LUMO below the main π^* peak of phenanthrene. However, we see that this LUMO is much weaker, broader, and lower energy than that appearing in K_3:anthracene and this trend is further supported by the experimental measurements.

Our justification for these shifts is as follows: in undoped molecular systems the lack of free charge carriers prevents efficient screening of the core hole, which causes a localized shift of the UMO states to lower energies for the x-ray transition, whereas the occupied states remain relatively unperturbed. On the other hand, K-doping not only adds charge carriers but also increases the interaction between molecules. With each molecule less electronically isolated, the core holes can be efficiently screened in K_3:phenanthrene and K_3:anthracene, reducing any localized energy shifts that may occur as a result of the x-ray transition. Our measurements therefore reveal not only increased conductivity, but also the increased intermolecular interaction responsible for why K_3:phenanthrene is vacuum compatible even though pure phenanthrene is not.

Conclusions

We have experimentally and theoretically studied the electronic structure of phenanthrene, anthracene, K_3:phenanthrene, and K_3:anthracene. We find that intercalating anthracene and phenanthrene with alkali metals causes the excitations of the system to behave more like those of a bulk crystal than a molecular solid, and causes the LUMOs to shift to lower energy levels, giving rise to improved conductivity and efficient core hole screening. Our calculations

show phenanthrene to change from a large band gap semiconductor to a conductor with potassium doping whereas anthracene merely has it's band gap reduced. This indicates that phenanthrene is more receptive to changes in conductivity introduced by potassium doping than anthracene, making phenanthrene a better candidate for further studies despite the structural and crystalline similarities between the two molecules.

Acknowledgement

This work was supported by the Natural Sciences and Engineering Research Council of Canada (NSERC) and the Canada Research Chair program. We gratefully acknowledge the assistance from the staff of the Canadian Light Source. This work was done with the partial support of the Ministry of Science and Education of the Russian Federation (State Contract No. 16.513.11.3007) and the Ural Division of the Russian Academy of Sciences (Project 12-I-2-2040). The Canadian Light Source is supported by NSERC, the National Research Council (NRC) Canada, the Canadian Institute of Health Research (CIHR), the Province of Saskatchewan, Western Economic Diversification Canada, and the University of Saskatchewan. The computational part of the research made use of resources from WestGrid and Compute/Calcul Canada.

Bibliography

Please note that all references contained in this thesis (including those from the above manuscript) can be found at the end of document.

6.2 Li_2RuO_3

I have contributed to another project that also resulted in publication during my time as a graduate student. X-ray spectroscopy and local density approximation calculations are used to study the electronic structure of Li_2RuO_3. Relative success in the study of the electronic and magnetic properties of hexagonal iridates prompted the study of Li_2RuO_3 which has a similar crystal structure based on $4d$ and $5d$ transition metals.

My work focused around taking the experimental data and calibrating it based on well-known absorption edges. I provided limited contribution to the manuscript in the form of revision and editing. Overall, this work amounted to approximately two weeks worth of work. Since this amounts to such a small percentage of my time as a graduate student, I am not including the manuscript. The manuscript was published in Physical Review B in March 2015. It can be found using the reference: Z. V. Pchelkina, A. L. Pitman, A. Moewes, E. Z. Kurmaev, Teck-Yee Tan, D. C. Peets, Je-Geun Park, and S. V. Streltsov. Electronic structure of Li_2RuO_3 studied by LDA and LDA+DMFT calculations and soft x-ray spectroscopy. *Phys. Rev. B.* **91**, 115138.

Chapter 7

Conclusions and Future Work

There is no greater education than one that is self-driven.

– NEIL DEGRASSE TYSON

At the onset of this thesis, we introduced the theme for the work contained – to develop and improve materials for use in electronics. In tuning the theme to apply only to materials containing transition metals, we found two major categories on which to focus our attention. First, materials that could be used in spintronics applications, namely, dilute magnetic semiconductors. Second, optoelectronics materials that traditionally feature larger band gaps. In applying the theme to molecular materials, we examined two different materials, each showing vastly different novel properties. Although our work certainly addressed all of these categories fitting into the overall theme, there are still many opportunities for future work. Below we summarize the findings of each project and present possible avenues for future work on the specific systems and their general classes of materials.

7.1 Conclusions

As mentioned above, the main goal of this work was in discovering novel properties of materials that either incorporate transition metals into their structure or are molecular by nature. We generalize this goal into three variants: materials that have a transition metal impurity; materials that are naturally comprised of transition metals and another constituent element (i.e., transition metal oxides); and materials that are naturally molecular systems.

After introducing the background material required for understanding our experiment and analysis, we introduced a system where transition metal atoms are added into a host lattice in the form of an impurity. For the last several years, this has been the primary method for testing the appearance of those novel properties required for spintronics applications. Those novel properties are primarily the appearance of ferromagnetic behaviour (through the dopant) along with a semiconducting band gap (via the host lattice). Our work confirmed the ability to determine the local bonding environment of the transition metal atom through matching multiplet calculations with the metal $L_{2,3}$ XAS and RIXS. Overall we saw that although Co:MoS_2 failed to provide the necessary semiconducting properties after the addition of Co, some unexpected features arose that may have usefulness elsewhere.

A somewhat less common experiment, the second variant treated a transition metal oxide with axial pressure. This grouping of materials is primarily intended for use in optoelectronics where tuning band gaps is important for selecting a specific band gap for a specific application. After examining the experimental data, we saw that pressure treated CuO was an excellent semiconductor with a variable band gap. More specifically, the band gap opened with increasing pressure, which is a stable trend for the samples tested. Finally, it is encour-

aging to see that the changes in the band gap due to pressure have little to no effect on the transition metal spectral shape, indicating that the other properties remain unaffected.

Finally, we examined the electronic structures for two different molecular systems: 1) potassium-doped phenanthrene and anthracene; and 2) Li_2RuO_3, a hexagonal iridate. Overall, these results focus on modelling the electronic structure using density functional theory and both found success, which is encouraging and allows us to better describe and predict similar systems.

7.2 Future Work

Above we presented work on several projects that gave some surprising, but useful conclusions. However, there are still a number of areas where our understanding of these systems can be expanded and reiterated. Below we present a few possible directions for additional investigation for each of the systems.

7.2.1 Dilute Magnetic Semiconductors

Additional work for dilute magnetic semiconductors generally takes on two forms: trying new combinations of transition metals and semiconductors; and performing additional experiments on known combinations. We recommend further investigation of the $Mo_{1-x}Co_xS_2$ system. First, an exploration covering a wider range of cobalt concentrations at finer intervals would be important to fully describe the system. Exploring other cobalt concentrations using the same experimental process presented in this work may introduce some novel properties that we did not reveal. Second, a study of this system's magnetic behaviour is important for

determining if the system has applications in other areas than spintronics.

7.2.2 Band Gap Engineering

Our work in band gap engineering was centred around the pressure treated CuO system. Again, two main avenues exist that may provide new and industry-changing discoveries. Given the relative success of the CuO system when treated with high axial pressure, it would be prudent to treat CuO with an extended range of pressures as a way to fully describe the system in the hope that boundaries or a general trend can be better defined. Next, the high pressure treatment could be easily applied to other transition metal oxides and tested in the same manner as this work to determine if the ability to tune the band gap is universal to this class of materials, or unique to copper (II) oxide.

7.2.3 Molecular Systems

For both molecular systems studied, further work would explore additional variations of the systems as well as begin testing the properties that inspired the work in the first place. In the case of the potassium-doped hydrocarbons, superconductivity or general conductivity tests would help to further define the system. Other variants of the Li_2RuO_3 system using alternate $4d$ and $5d$ transition metals in place of Ru may result in a large number of these materials following this crystal structure, all having exotic magnetic properties.

References

[1] Shockley, W. The path to the conception of the junction transistor. *IEEE Trans. Electron Devices* **23**, 597–620 (1976).

[2] Moore, G. E. *Moore's law at 40.* Understanding Moore's Law: Four Decades of Innovation (Chemical Heritage Foundation, 2006).

[3] Wolf, S. A. *et al.* Spintronics: A spin-based electronics vision for the future. *Science* **294**, 1488 (2001).

[4] Felser, C., Fecher, G. H. & Balke, B. Spintronics: A challenge for materials science and solid-state chemistry. *Angew. Chem. Int. Ed.* **45**, 668 (2007).

[5] Pearton, S. J. *et al.* Wide band gap ferromagnetic semiconductors and oxides. *J. App. Phys.* **93**, 1 (2003).

[6] MacDonald, A. H., Schiffer, P. & Samarth, N. Ferromagnetic semiconductors: moving beyond (Ga,Mn)As. *Nat. Mater.* **4**, 195 (2005).

[7] Ohno, H. *et al.* (Ga,Mn)As: A new diluted magnetic semiconductor based on GaAs. *App. Phys. Lett.* **69**, 363 (1996).

[8] Pearton, S. J., Heo, W. H., Ivill, M., Norton, D. P. & Steiner, T. Dilute magnetic semiconducting oxides. *Semicond. Sci. Technol.* **19**, R59 (2004).

[9] Sato, K. *et al.* First-principles theory of dilute magnetic semiconductors. *Rev. Mod. Phys.* **82**, 1633 (2010).

[10] Dietl, T. A ten-year perspective on dilute magnetic semiconductors and oxides. *Nat. Mater.* **9**, 965 (2010).

[11] Wilson, J. A. & Yoffe, A. D. The transition metal dichalcogenides discussion and interpretation of the observed optical, electrical and structural properties. *Adv. Phys.* **18**, 193 (1969).

[12] Ramasubramaniam, A. Large excitonic effects in monolayers of molybdenum and tungsten dichalcogenides. *Phys. Rev. B* **86**, 115409 (2012).

[13] Wang, Q. H., Kalantar-Zadeh, K., Kis, A., Coleman, J. N. & Strano, M. S. Electronics and optoelectronics of two-dimensional transition metal dichalcogenides. *Nat. Nano.* **7**, 699 (2012).

[14] Yadgarov, L. *et al.* Controlled doping of MS_2 (M=W, Mo) nanotubes and fullerene-like nanoparticles. *Angew. Chem. Int. Ed.* **51**, 1148 (2012).

[15] Hsu, W. K. *et al.* Titanium-doped molybdenum disulfide nanostructures. *Adv. Funct. Mater.* **11**, 69 (2001).

[16] Durbin, T. D., Lince, J. R. & Yarmoff, J. A. Chemical interaction of thin Cr films with the $MoS_2(0001)$ surface studied by x-ray photoelectron spectroscopy and scanning Auger microscopy. *J. Vac. Sci. Technol., A* **10**, 2529 (1992).

[17] Lince, J. R., Carré, D. J. & Fleischauer, P. D. Schottky-barrier formation on a covalent semiconductor without Fermi-level pinning: The metal-$MoS_2(0001)$ interface. *Phys. Rev. B* **36**, 1647 (1987).

[18] Ramasubramaniam, A. & Naveh, D. Mn-doped monolayer MoS_2: An atomically thin dilute magnetic semiconductor. *Phys. Rev. B* **87**, 195201 (2013).

[19] Mott, N. F. . The basis of the electron theory of metals, with special reference to the transition metals. *Proc. Phys. Soc. London, Sect. A* **62**, 416 (1949).

[20] Mott, N. F. On the transition to metallic conduction in semiconductors. *Can. J. Phys.* **34**, 1356 (1956).

[21] Mott, N. F. The transition to the metallic state. *Philos. Mag.* **6**, 287 (1961).

[22] Hubbard, J. Electron correlations in narrow energy bands. II. The degenerate band case. *Proc. R. Soc. London, Ser. A* **277**, 237 (1964).

[23] Hubbard, J. Electron correlations in narrow energy bands. III. An improved solution. *Proc. R. Soc. London, Ser. A* **281**, 401 (1964).

[24] Stöhr, J. *NEXAFS Spectroscopy* (Springer-Verlag, 1992).

[25] Ebert, H., Stöhr, J., Parkin, S. S. P., Samant, M. & Nilsson, A. *L*-edge x-ray absorption in fcc and bcc Cu metal: Comparison of experimental and first-principles theoretical results. *Phys. Rev. B* **53**, 16067 (1996).

[26] Green, R. J. *Transition metal impurities in semiconductors: Induced magnetism and band gap engineering.* Ph.D. thesis, University of Saskatchewan (2013).

[27] de Groot, F. Multiplet effects in x-ray spectroscopy. *Coord. Chem. Rev.* **249**, 31 (2005).

[28] Cowan, R. D. *The Theory of Atomic Structure and Spectra* (University of California Press, 1981).

[29] de Groot, F. & Kotani, A. *Core Level Spectroscopy of Solids* (Taylor & Francis, 2008).

[30] Kotani, A. & Shin, S. Resonant inelastic x-ray scattering spectra for electrons in solids. *Rev. Mod. Phys.* **73**, 203 (2001).

[31] Ament, L. J. P., van Veenendaal, M., Devereaux, T. P., Hill, J. P. & van den Brink, J. Resonant inelastic x-ray scattering studies of elementary excitations. *Rev. Mod. Phys.* **83**, 705 (2011).

[32] Muir, D. & He, F. 10ID-2 Resonant Elastic and Inelastic X-ray Scattering (REIXS) Beamline - Beamline Design (2015). URL `http://exshare.lightsource.ca/REIXS/Pages/BLDesign.aspx`.

[33] Thole, B. T., Cowan, R. D., Sawatzky, G. A., Fink, J. & Fuggle, J. C. New probe for the ground-state electronic structure of narrow-band and impurity systems. *Phys. Rev. B* **31**, 6856 (1985).

[34] Sakurai, J. J. *Advanced Quantum Mechanics* (Addison-Wesley Publishing, 1967).

[35] Tulkki, J. & Aberg, T. Statistical theory of electronic Raman resonance scattering by oriented atoms. *J. Phys. B: At. Mol. Phys.* **13**, 3341 (1980).

[36] Tulkki, J. & Aberg, T. Behaviour of Raman resonance scattering across the K x-ray absorption edge. *J. Phys. B: At. Mol. Phys.* **15**, L435 (1982).

[37] Hunt, A., Muir, D. & Moewes, A. Studying $4d$–$4f$ transitions in Er using resonant inelastic scattering. *J. Electron. Spectrosc. Relat. Phenom.* **144**, 573 (2005).

[38] Moewes, A., Postnikov, A. V., Kurmaev, E. Z., Grush, M. M. & Ederer, D. L. Resonant mixing of widely separated intermediate states and charge transfer at the $4d$–$4f$ resonance of La compounds. *Europhys. Lett.* **49**, 665 (2000).

[39] Bethe, H. Thermal division in crystals. *Ann. Phys. (Berlin)* **3**, 133 (1929).

[40] Ballhausen, C. J. *Introduction to Ligand Field Theory* (McGraw-Hill Book Co., 1962).

[41] Ghiringhelli, G. *et al.* NiO as a test case for high resolution resonant inelastic soft x-ray scattering. *J. Phys. Condens. Matter* **17**, 5397 (2005).

[42] Chiuzbăian, S. *et al.* Combining M- and L-edge resonant inelastic x-ray scattering for studies of 3d transition metal compounds. *Phys. Rev. B* **78**, 245102 (2008).

[43] Ghiringhelli, G. *et al.* Resonant inelastic x-ray scattering of MnO: $L_{2,3}$ edge measurements and assessment of their interpretation. *Phys. Rev. B* **73**, 035111 (2006).

[44] Magnuson, M., Butorin, S., Guo, J.-H. & Nordgren, J. Electronic structure investigation of CoO by means of soft x-ray scattering. *Phys. Rev. B* **65**, 205106 (2002).

[45] Magnuson, M., Butorin, S. M., Agui, A. & Nordgren, J. Resonant soft x-ray Raman scattering of NiO. *J. Phys. Condens. Matter* **14**, 3669 (2002).

[46] Gmelin, L. *Gmelin Handbook of Inorganic and Organometallic Chemistry*, vol. B7 (Springer-Verlag, Berlin, 1995), 8th edn. URL `http://www.lib.utexas.edu/chem/info/gmelin.html`.

[47] Kam, K. K. & Parkinson, B. A. Detailed photocurrent spectroscopy of the semiconducting group VIB transition metal dichalcogenides. *J. Phys. Chem.* **86**, 463 (1982).

[48] Ramakrishna Matte, H. S. S. *et al.* Mos2 and ws2 analogues of graphene. *Angewandte Chemie* **122**, 4153 (2010). URL `http://dx.doi.org/10.1002/ange.201000009`.

[49] Wu, N. *et al.* The electronic band structure of cos_2. *Journal of Physics: Condensed Matter* **19**, 156224 (2007).

[50] Antonov, V. N., Andryushchenko, O. V., Shpak, A. P., Yaresko, A. N. & Jepsen, O. Electronic structure, optical spectra, and x-ray magnetic circular dichroism in cos_2. *Phys. Rev. B* **78**, 094409 (2008).

[51] Green, R. J. *et al.* Identifying local dopant structures and their impact on the magnetic properties of spintronic materials. *Phys. Rev. B* **83**, 115207 (2011).

[52] Hardee, K. L. & Bard, A. J. Semiconductor electrodes x . photoelectrochemical behavior of several polycrystalline metal oxide electrodes in aqueous solutions. *J. Electrochem. Soc.* **124**, 215 (1977).

[53] Shen, S.-C. Wide-bandgap device research and development at SRL (2011). URL `http://users.ece.gatech.edu/ shensc/research.html`.

[54] Forrest, S. R. The path to ubiquitous and low-cost organic electronic appliances on plastic. *Nature* **428**, 911 (2004).

[55] Gershenson, M. E., Podzorov, V. & Morpurgo, A. F. Electronic transport in single-crystal organic transistors. *Rev. Mod. Phys.* **78**, 973 (2006).

[56] Baldo, M. A. *et al.* Highly efficient phosphorescent emission from organic electroluminescent devices. *Nature* **395**, 151 (1998).

[57] Friend, R. H. *et al.* Electroluminescence in conjugated polymers. *Nature* **397**, 121 (1999).

[58] Peumans, P., Uchida, S. & Forrest, S. R. Efficient bulk heterojunction photovoltaic cells using small-molecular-weight organic thin films. *Nature* **425**, 158 (2003).

[59] Li, G. *et al.* High-efficiency solution processable polymer photovoltaic cells by self-organization of polymer blends. *Nat. Mater.* **4**, 864 (2005).

[60] Hayakawa, H., Yoshikawa, N., Yorozu, S. & Fujimaki, A. Superconducting digital electronics. *Proc. IEEE* **92**, 1549 (2004).

[61] Morrow, G. Progress in mri magnets. *IEEE Trans. Appl. Supercond.* **10**, 744 (2000).

[62] Hassenzahl, W. V. *et al.* Electric power. applications of superconductivity. *Proc. IEEE* **92**, 1655 (2004).

[63] Roth, F., Bauer, J., Mahns, B., Büchner, B. & Knupfer, M. Electronic structure of undoped and potassium-doped coronene investigated by electron energy-loss spectroscopy. *Phys. Rev. B* **85**, 014513–1 (2012).

[64] Hebard, A. F. *et al.* Superconductivity at 18k in potassium-doped C_{60}. *Nature* **350**, 600 (1991).

[65] Emery, N. *et al.* Superconductivity of bulk CaC_6. *Phys. Rev. Lett.* **95**, 087003–1 (2005).

[66] Lu, D., Yan, X. H. & Xiao, Y. Charge distribution of a potassium-doped combined system of graphene and hexagonal boron nitride. *Solid State Commun.* **151**, 1771 (2011).

[67] Salvato, M. *et al.* Effect of potassium doping on electrical properties of carbon nanotube fibers. *Phys. Rev. B* **84**, 233406–1 (2011).

[68] Weller, T. E., Ellerby, M., Saxena, S. S., Smith, R. P. & Skipper, N. T. Superconductivity in the ytterbium intercalated graphite compounds C_6Yb and C_6Ca. *Nat. Phys.* **1**, 39 (2005).

[69] Tanigaki, K. *et al.* Superconductivity at 33 k in $cs_xrb_yC_{60}$. *Nature* **352**, 222 (1991).

[70] Kubozono, Y. *et al.* Metal-intercalated aromatic hydrocarbons: A new class of carbon-based superconductors. *Phys. Chem. Chem. Phys.* **13**, 16476 (2011).

[71] Mitsuhashi, R. *et al.* Superconductivity in alkali-metal-doped picene. *Nature* **464**, 76 (2010).

[72] Cudazzo, P. *et al.* Plasmon dispersion in molecular solids: Picene and potassium-doped picene. *Phys. Rev. B* **84**, 155118–1 (2011).

[73] Kosugi, T., Miyake, T., Ishibashi, S., Arita, R. & Aoki, H. First-principles structural optimization and electronic structure of the superconductor picene for various potassium doping levels. *Phys. Rev. B* **84**, 214506–1 (2011).

[74] Kosugi, T., Miyake, T., Ishibashi, S., Arita, R. & Aoki, H. First-principles electronic structures of solid picene. *J. Phys. Soc. Jpn* **78**, 113704–1 (2009).

[75] Roth, F., Mahns, B., Büchner, B. & Knupfer, M. Dynamic response and electronic structure of potassium-doped picene investigated by electron energy-loss spectroscopy. *Phys. Rev. B* **83**, 144501–1 (2011).

[76] Wang, X. F. *et al.* Superconductivity at 5k in potassium doped phenanthrene. *Nat. Commun.* **2**, 507–1 (2011).

[77] Hähner, G. Near Edge X-Ray Absorption Fine Structure Spectroscopy as a Tool to Probe Electronic and Structural Properties of Thin Organic Films and Liquids. *Chem. Soc. Rev.* **35**, 1244 (2006).

[78] Regier, T. *et al.* Performance and capabilities of the canadian dragon: The sgm beamline at the canadian light source. *Nucl. Instrum. Methods Phys. Res. A* **582**, 93 (2007).

[79] Hermann, K. *et al.* Stobe-demon: Stockholm-berlin version of demon, a density functional theory molecule/cluster package (2007). Version 3.0.

[80] Becke, A. D. Density-functional exchange-energy approximation with correct asymptotic behavior. *Phys. Rev. A* **38**, 3098 (1988).

[81] Perdew, J. P. & Wang, Y. Accurate and simple density functional for the electronic exchange energy: Generalized gradient approximation. *Phys. Rev. B* **33**, 8800 (1986).

[82] Blaha, P., Schwarz, K., Madsen, G. K. H., Kvasnicka, D. & Luitz, J. Wien2k, an augmented plane wave + local orbitals program for calculating crystal properties (2001). Karlheinz Schwarz, Techn. Universität, Wien, ISBN 3-9501031-1-2.

[83] Trotter, J. The crystal and molecular structure of phenanthrene. *Acta Cryst.* **16**, 605 (1963).

[84] Cruickshank, D. W. J. A detailed refinement of the crystal and molecular structure of anthracene. *Acta Cryst.* **9**, 915 (1956).

[85] de Andres, P. L., Guijarro, A. & Vergés, J. A. Crystal structure and electronic states of K_3picene. *Phys. Rev. B.* **84**, 144501–1 (2011).

[86] Schwarz, K., Neckel, A. & Nordgren, J. On the x-ray emission spectra from FeAl. *J. Phys. F: Met. Phys.* **9**, 2509 (1979).

[87] Minkov, I. *et al.* Core excitations of naphthalene: Vibrational structure versus chemical shifts. *J. Chem. Phys.* **121**, 5733 (2004).

[88] Gordon, M. L. *et al.* Inner-shell excitation spectroscopy of fused-ring aromatic molecules by electron energy loss and x-ray raman technique. *J. Phys. Chem. A* **107**, 8512 (2003).

[89] Perger, W. F. Calculation of band gaps in molecular crystals using hybrid functional theory. *Chem. Phys. Lett.* **368**, 319 (2003).

[90] Vaubel, G. & Baessler, H. Determination of the band-gap in anthracene. *Phys. Lett. A* **27**, 328 (1968).

[91] Tóbik, J., Dal Corso, A., Scandolo, S. & Tosatti, E. Organic molecular crystals in electric fields. *Surf. Sci.* **566–568**, 644 (2004).

[92] Bhatti, M. T., Ali, M., Shahid, G. N. & Saleh, M. Characterization of phenanthrene single crystals. *Turk. J. Phy.* **24**, 673 (2000).